Theoretical Analysis of the Ca^{2+} Spark Amplitude Distribution

Leighton T. Izu,* W. Gil Wier,# and C. William Balke*#
*Department of Medicine, Division of Cardiology, and #Department of Physiology, University of Maryland School of Medicine, Baltimore, Maryland 21201 USA

ABSTRACT A difficulty of using confocal microscopy to study Ca^{2+} sparks is the uncertainty of the linescan position with respect to the source of Ca^{2+} release. Random placement of the linescan is expected to result in a broad distribution of measured Ca^{2+} spark amplitudes (*a*) even if all Ca^{2+} sparks were generated identically. Thus variations in Ca^{2+} spark amplitude due to positional differences between confocal linescans and Ca^{2+} release site are intertwined with variations due to intrinsic differences in Ca^{2+} release properties. To separate these two sources of variations on the Ca^{2+} spark amplitude, we determined the effect changes of channel current or channel open time—collectively called the source strength, α—had on the measured Ca^{2+} spark amplitude histogram, $N(a)$. This was done by 1) simulating Ca^{2+} release, Ca^{2+} and fluo-3 diffusion, and Ca^{2+} binding reactions; 2) simulation of image formation of the Ca^{2+} spark by a confocal microscope; and 3) using a novel automatic Ca^{2+} spark detector. From these results we derived an integral equation relating the probability density function of source strengths, $f_\alpha(\alpha)$, to $N(a)$, which takes into account random positional variations between the source and linescan. In the special, but important, case that the spatial distribution of Ca^{2+}-bound fluo-3 is Gaussian, we show the following: 1) variations of Ca^{2+} spark amplitude due to positional or intrinsic differences can be separated, and 2) $f_\alpha(\alpha)$ can, in principle, be calculated from the Ca^{2+} spark amplitude histogram since $N(a)$ is the sum of shifted hyperbolas, where the magnitudes of the shifts and weights depend on $f_\alpha(\alpha)$. In particular, if all Ca^{2+} sparks were generated identically, then the plot of $1/N(a)$ against *a* will be a straight line. Multiple populations of channels carrying distinct currents are revealed by discontinuities in the $1/N(a)$ plot. 3) Although the inverse relationship between Ca^{2+} spark amplitude and decay time might be used to distinguish Ca^{2+} sparks from different channel populations, noise can render the measured decay times meaningless for small amplitude Ca^{2+} sparks.

INTRODUCTION

Calcium (Ca^{2+}) "sparks" are brief, spatially localized Ca^{2+} release events resulting from the opening of one or a cluster of sarcoplasmic reticulum (SR) Ca^{2+} release channels. The combination of laser scanning confocal microscopy and the fluorescent Ca^{2+} indicator, fluo-3, has revealed Ca^{2+} sparks in single cardiac cells (Cheng et al., 1993; López-López et al., 1995), cardiac trabeculae (Wier et al., 1997), skeletal muscle cells (Tsugorka et al., 1995; Klein et al., 1996), and smooth muscle cells (Nelson et al., 1995).

The observation of spontaneous Ca^{2+} sparks (Cheng et al., 1993) and the description of the voltage dependence of evoked Ca^{2+} sparks (López-López et al., 1995; Cannell et al., 1995) provided important experimental support for the local control theory of cardiac excitation-contraction coupling (Stern, 1992). It is now generally accepted that Ca^{2+} current through L-type Ca^{2+} channels locally triggers SR Ca^{2+} release. Evidence for this comes indirectly from measurements of Ca^{2+} sparks under whole cell voltage clamp (López-López et al., 1994, 1995; Santana et al., 1996) and more directly from measurements of Ca^{2+} sparks localized to the region under a cell-attached membrane patch (Shorofsky et al., 1998).

While the trigger for SR Ca^{2+} release is understood, how the release is controlled is still unclear. A myriad of factors appear to control SR Ca^{2+} release. For example, 1) SR load affects both the probability of Ca^{2+} spark occurrence and the Ca^{2+} spark amplitudes (Satoh et al., 1997; Györke et al., 1997; Song et al., 1997); 2) the number of SR Ca^{2+} release channels opening to generate a Ca^{2+} spark might be variable (Lipp and Niggli, 1996) and produce Ca^{2+} sparks of different amplitudes (Parker and Wier, 1996); 3) the SR Ca^{2+} release channel appears to have a subconductance that results in two populations of Ca^{2+} sparks with different amplitudes (Cheng et al., 1993; Xiao et al., 1997); 4) Ca^{2+} sparks can trigger other Ca^{2+} sparks (Klein et al., 1996; Parker et al., 1996; Blatter et al., 1997), that might appear as population of Ca^{2+} sparks with different amplitudes (Klein et al., 1996); and 5) the proportion of Ca^{2+} sparks in different amplitude populations appears to be altered in certain disease states (Shorofsky et al., 1996, 1997).

To better understand the mechanisms underlying the control of Ca^{2+} release we need to estimate the current through the SR Ca^{2+} release channel, but this current cannot be measured directly in an intact cell and must be estimated from the amplitude of the Ca^{2+} spark. This estimate is complicated by 1) the kinetics and capacity of Ca^{2+} buffering by endogenous Ca^{2+} buffers and exogenous Ca^{2+} buffers, such as the Ca^{2+} indicator fluo-3 (Balke et al., 1994; Smith et al., 1996); 2) the diffusion properties of free Ca^{2+} and mobile Ca^{2+} buffers (Wagner and Keizer, 1994; Smith et al., 1996); and 3) the uncertainty of the distance between the site of Ca^{2+} release and the position of the

Received for publication 6 February 1998 and in final form 8 June 1998.
Address reprint requests to C. William Balke, M.D., University of Maryland School of Medicine, Department of Physiology, Room 544, Howard Hall, 660 W. Redwood St., Baltimore, MD 21201. Tel.: 410-706-0515; Fax: 410-706-8610; E-mail: bbalk001@umaryland.edu.

0006-3495/98/09/1144/19 $2.00

confocal linescan (Pratusevich and Balke, 1996; Shirokova and Ríos, 1997).

Pratusevich and Balke (1996) showed that the random placement of the confocal linescan relative to the Ca^{2+} release sites results in a broad distribution of measured Ca^{2+} spark amplitudes even if all Ca^{2+} sparks were generated identically. Thus it becomes difficult to distinguish variations in Ca^{2+} spark amplitude due to *intrinsic* variations in SR Ca^{2+} release channel current from *positional* variations arising from varying distance between the confocal linescan and the site of Ca^{2+} release. In this paper we show, in theory, that variations in Ca^{2+} spark amplitude arising from intrinsic and positional changes can be separated. We do this by deriving an integral equation that gives the relationship between the probability distribution of source strengths (SR Ca^{2+} release channel current or channel open time) and the Ca^{2+} spark amplitude histogram. This integral equation takes into account the effect of positional variations on the Ca^{2+} spark amplitude histogram. The integral equation can be solved analytically, allowing us to explicitly solve for the probability distribution of source strengths when given the measured spark amplitude histogram. In this way the variations in Ca^{2+} spark amplitude due to intrinsic and positional changes, which are intertwined in the amplitude histogram, can be separated.

METHODS

To understand the relationship between the measured Ca^{2+} spark properties and the underlying events we need to simulate the processes that influence the formation of the Ca^{2+} spark. These processes are (1) the release of Ca^{2+} from the SR by the opening of a Ca^{2+} release channel; (2) the diffusion of Ca^{2+} into the cytoplasm; (3) the reaction of Ca^{2+} with endogenous buffers, such as troponin-C, and the fluorescent Ca^{2+} indicator fluo-3; (4) the formation of the optical image of the Ca^{2+}-bound fluo-3 dye; (5) the generation of a linescan image from the optical signal; (6) the generation of random fluctuations of the fluorescent signal due to photon and other sources of noise; and (7) the detection of the Ca^{2+} spark.

Reaction-diffusion equations

Processes (1), (2), and (3) are captured in the set of partial differential equations describing the reaction of Ca^{2+} with buffers and the diffusion of Ca^{2+} in the cytoplasm. The solution of these equations gives the 3-dimensional distribution of the Ca^{2+}-bound fluo-3 as a function of time.

The chemical species included in the model equations are Ca^{2+} (concentration denoted by C), immobile endogenous buffers both free (F_b) and bound to Ca^{2+} (G_b), mobile fluo-3 (free F_m, bound G_m), and immobilized fluo-3 (free F_i, bound G_i). Mass transport of Ca^{2+} and mobile fluo-3 is assumed to follow Fick's law and the reaction rates (R_j) are governed by mass action kinetics. Thus the reaction rate between Ca^{2+} and any buffer is given by

$$R_j = -k_j^+ C F_j + k_j^- G_j, \tag{1}$$

where $j = i$, m, or b and k_j^+ and k_j^- are the forward and reverse rate constants, respectively.

We also make the following assumptions: (1) Ca^{2+} released from the SR is approximated by a point source; (2) both reaction and diffusion occur radially symmetrically; (3) the diffusion coefficients of the Ca^{2+}-bound mobile fluo-3 and the free mobile fluo-3 are identical; and (4) before the opening of the Ca^{2+} channel, all chemical species are at their steady-state value and there are no spatial gradients.

Under these assumptions the reaction-diffusion equations are

$$\frac{\partial C}{\partial t} = D_C \nabla^2 C + \sum_j R_j(C, F_j, H_j) + J_{SR}\delta(r) \tag{2}$$

$$\frac{\partial F_m}{\partial t} = D_m \nabla^2 F_m + R_m(C, F_m, H_m) \tag{3}$$

$$\frac{\partial F_i}{\partial t} = R_i(C, F_i, H_i) \tag{4}$$

$$\frac{\partial F_b}{\partial t} = R_b(C, F_b, H_b), \tag{5}$$

where

$$R_j(C, F_j, H_j) = -k_j^+ C F_j + k_j^-(H_j - F_j) \tag{6}$$

and

$$H_j = F_j + G_j. \tag{7}$$

The Laplacian operator ∇^2 for the radially symmetric domains is

$$\nabla^2 = \frac{\partial^2}{\partial r^2} + \frac{2}{r}\frac{\partial}{\partial r}. \tag{8}$$

The point source of Ca^{2+} release by the SR is located at the origin and is given by $J_{SR}\delta(r)$, where $\delta(r)$ is the Dirac delta-function. J_{SR} is related to the Ca^{2+} release channel current I_{SR} by $J_{SR} = I_{SR}/(z\mathcal{F})$ where $z = 2$ is the Ca^{2+} valence and $\mathcal{F}$ is Faraday's constant. A typical value of I_{SR} is 1.4 pA.

The reason there are no equations for G_j is because under assumption (3) the sum H_j satisfies the *linear* diffusion equation $\partial H_j/\partial t = D_j \nabla^2 H_j$, and under assumption (4) the initial condition satisfies $H_j(r, 0) = \bar{H}_j$ = constant, so the diffusion equation has the solution $H_j(r, t) \equiv \bar{H}_j$. Accordingly, F_j and G_j satisfy the algebraic relationship $G_j = H_j - F_j = \bar{H}_j - F_j$.

For simplicity, we did not include a Ca^{2+} pump in the model because others (Gómez et al., 1996) found that 80% of the decline of the Ca^{2+} fluorescence signal could be accounted for by diffusion and buffering.

The diffusion coefficient for Ca^{2+} was set to 6×10^{-6} cm^2/s. The apparent diffusion coefficient of fluo-3 is found to be 0.2×10^{-6} cm^2/s in frog skeletal muscle, which is about a factor of 5 times smaller than predicted from its molecular weight (Harkins et al., 1993). To account for this difference Harkins et al. (1993) estimated that 78% of the dye is bound to immobile myoplasmic constituents and only 22% is freely mobile. In our simulations the ratio of concentrations (β) of immobile to mobile fluo-3, β was set to 5 or in some cases 2. This latter value comes from prior determination of the ratio of immobile to mobile fura-2 in guinea pig heart cells (Blatter and Wier, 1990). D_m was set to 0.9×10^{-6} cm^2/s. The free mobile fluo-3 concentration was fixed to 50 μM in all simulations.

The rate-limiting step of most reactions involving Ca^{2+} is the dehydration of the calcium ion and is ~200–700/μM s (Hague, 1977). We chose a value for the forward rate constant k_m^+ to be near the middle of the range, 400/μM s. The reverse rate constant, k_m^- = 160/s, was calculated using the dissociation constant value of 400 nM.

The total concentration of endogenous buffers $\bar{H}_b$ was set to 123 μM (Berlin et al., 1994). The forward rate constant k_b^+ was chosen to be 100/μM s and the reverse rate constant of k_b^- = 100/s to give the endogenous buffer dissociation constant of 1 μM, close to the value (0.96 μM) found by Berlin et al. (1994).

The experimental parameters were determined at room temperature (20–25°C) except for Harkins et al.'s estimate of $\beta = 5$, which was measured at 16°C. No temperature compensation was made.

Numerical solution

Eqs. 2–5 were solved using Facsimile (AEA Technologies, Harwell, UK), which solves each of the equations in the time variable on a workstation (RS 6000, IBM Corp., Armonk, NY). The spatial domain extending from $0 < r < L$ was discretized into N compartments of equal lengths $h = L/N$. The ith compartment is the spherical shell bounded by $r_i = ih$ and $r_{i+1} = (i + 1)h$. The time rate of change of the concentration in the ith compartment is

$$\frac{dc_i}{dt} = \frac{J_iA_i - J_{i+1}A_{i+1}}{\Delta V_i} + R_i, \quad i = 1, \ldots, N - 1, \quad (9)$$

where $A_i = 4\pi i^2h^2$ is the surface area of the sphere of radius r_i and $\Delta V_i = 4\pi h^3(i^2 + i + 1/3)$ is the volume between the spheres of radius r_i and r_{i+1}. R_i is the reaction term. J_i is given by Fick's law $J_i = -(D/h)(c_i - c_{i-1})$. The differential equation for the Nth compartment is derived similarly, but imposing the zero-flux boundary condition that requires the fictitious point $c_{N+1} = c_N$. For $i = 0$, which contains the point source, material balance yields

$$\frac{dc_0}{dt} = \frac{3D(c_1 - c_0)}{h^2} + \frac{J_{SR}}{V_0} + R_0 \quad (10)$$

where $V_0 = 4\pi h^3/3$.

We used $L = 6$ μm and $N = 600$. This code was tested on the linear problem obtained by setting all reaction terms to zero for which the analytic solution was available for comparison. Except at very early times following channel opening ($\sim$10 μs) the relative error was within 5% even at the smallest resolvable distance of $r = 0.015$ μm. In all simulations the concentration at $r = 6$ μm did not vary over the short (<200 ms) integration time so any of the usual boundary conditions (Dirichlet, Neumann, or Robin) would give essentially identical results.

Formation of the optical image

The Ca^{2+} spark is the optical image of the distribution of Ca^{2+}-bound fluo-3, $G_m(r, t) + G_i(r, t)$. Any optical instrument forms a blurred image of the object and the extent of the blurring is given by the instrument's point spread function (PSF). We used a 3-dimensional Gaussian function as the PSF of the confocal microscope

$$PSF(x, y, z) = N \exp(-x^2/\sigma_{xy}^2)\exp(-y^2/\sigma_{xy}^2)\exp(-z^2/\sigma_z^2), \quad (11)$$

where $N = (\sigma_{xy}^2\sigma_z\pi^{3/2})^{-1}$ normalizes the integral of the PSF over all space to unity. The standard deviation σ is related to the confocal full-width at half-maximum (FWHM) by $\sigma = \text{FWHM}/[2(\log 2)^{1/2}]$. A typical value for the lateral FWHM is $\text{FWHM}_{xy} = 0.4$ μm. Values for the axial FWHM range from 0.41 μm (Parker et al., 1997) to 1.3 (Pratusevich and Balke, 1996).

The intensity contributions to the image of the Ca^{2+}-bound fluo-3 at any point (x, y, z) measured from the point source at the origin is proportional to the convolution

$$I(x, y, z, t) = \int\int\int [G_m(x', y', z', t) + G_i(x', y', z', t)] \text{PSF}(x - x', y - y', z - z')dx'dy'dz'. \quad (12)$$

The convolution was carried out by multiplication of the discrete approximation of the Fourier transforms of $G_m + G_i$ and PSF then taking the inverse transform. The size of the volume to carry out the convolution was dictated by the extent of spreading of the bound indicator and the values of the axial and lateral FWHM. A typical computational volume (of 64^3 elements) measures 3.6 μm along the x- and y-directions and 4.5 μm in the z-direction.

Generating a linescan image

Generation of the linescan image of a Ca^{2+} spark starts by choosing the linescan position (y^*, z^*) in the $y - z$ plane, which is perpendicular to the linescan direction along x. Then for each time point t_j values of $I(x, y^*, z^*, t_j)$ for all x are collected. Stacking these one-dimensional arrays for all the computed times ($0 < t_j < 180$ ms) produces the linescan image of the Ca^{2+} spark. The length of the linescan image along x is 4 μm and 180 ms in time. This small linescan image is embedded in a larger array whose values are set to the image value of bound fluo-3 ($G_m + G_i$) at equilibrium. Additionally, multiple Ca^{2+} sparks can be embedded in the large array at random positions, with the constraint that Ca^{2+} sparks do not overlap. The result of this embedding is an image that looks qualitatively like a linescan image from a real confocal microscope. A sample image in which signal fluctuations have been added is shown in Fig. 1 *B*.

We created realistic linescan images because we wanted observers to identify these simulated Ca^{2+} sparks in order to study the role of subjective factors on Ca^{2+} spark identification.

Random fluctuations of the fluorescent signal

Random fluctuations of the fluorescent signals arise from the intrinsic granularity of photons and from electronic noise (Pawley, 1995). To accurately model noise in simulated confocal linescan images, we measured the noise properties in linescan images made from the homemade confocal microscope (Parker et al., 1997). The mean signal level and the standard deviation were calculated in a 10 × 10-pixel sample area in three regions: background, where the fluorescence intensity was low and uniform; regions containing a narrow band of elevated fluorescence at the site of the t-tubules (Shacklock et al., 1995; Klein et al., 1996); and at Ca^{2+} sparks. Fig. 2 shows that the standard deviation of the values in the sample areas increase linearly (slope = 0.3) with the mean fluorescence, and this linear relationship holds regardless of the sample region. Moreover, the distribution of noise values is approximately Gaussian (data not shown). We therefore added to the value of each point in our simulated linescan image a random number from a Gaussian distribution whose standard deviation was 0.3 times the value at that point.

Automatic detection of Ca^{2+} sparks

We developed a program to automatically identify Ca^{2+} sparks in linescan images. This program relieves the tedium of manually identifying Ca^{2+}

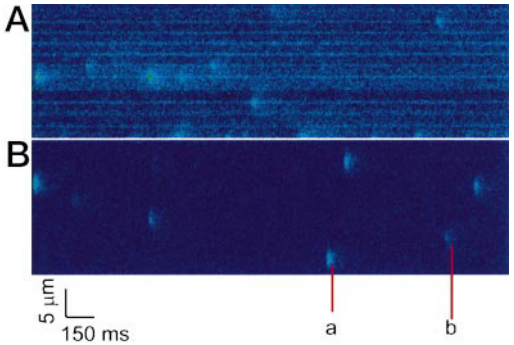

FIGURE 1 Comparison of an actual confocal linescan image (*A*) and a simulated linescan (*B*). Periodically spaced horizontal lines in (*A*) are located at the t-tubules and may represent inhomogeneous dye distribution. No dye inhomogeneities exist in the simulations, so the background is uniform in (*B*). The simulated Ca^{2+} sparks are qualitatively similar to real Ca^{2+} sparks. The number of Ca^{2+} sparks per linescan image was random. The space and time positions of the Ca^{2+} sparks were also random, but were constrained not to overlap. Ca^{2+} sparks labeled *a* and *b* arise from linescan positions marked in Fig. 3 *A*. Each pixel is 0.1 μm by 3 ms.

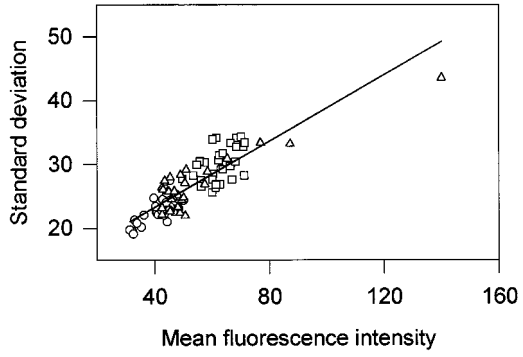

FIGURE 2 Statistical fluctuation measured by the standard deviation of fluorescence signal as a function of mean fluorescence level. Data were collected in a 10 × 10 pixel area in three regions: background (*circles*), t-tubular region (*squares*), and Ca^{2+} sparks (*triangles*). Measurements were made on linescan images collected using the homemade confocal microscope. The best fit line has a slope of 0.3.

sparks and ensures a more consistent choice of Ca^{2+} sparks than might be achieved by observers. This program identifies as Ca^{2+} sparks regions that have a sufficiently high *density* of pixels that exceed some threshold level. Identification of Ca^{2+} sparks starts by creating a binary image in which all pixels in an image whose value is less than the background level + threshold are set to zero, and all other pixels to unity. The threshold equals the standard deviation of the background signal times a factor (typically 1.4) that can be varied by the user.

High density regions of non-zero pixels are identified by using the following procedure iteratively. At every pixel in the image (i, j), the number of non-zero pixels within a square neighborhood of size N_{size} centered on (i, j) are counted. If this number is less than N_{live}, then the (i, j) pixel is set to 0 (i.e., the pixel "dies"); otherwise it is set to 1 (i.e., the pixel "survives" or is "born"). This procedure is repeated $N_{generation}$ times for every pixel. As the notation suggests, this algorithm is based on ideas gleaned from modeling density-dependent population growth using cellular automata. Although the procedure appears slow and tedious, it in fact runs quickly with the array-oriented programming language IDL (Research Systems, Inc., Boulder, CO). The number of "live" neighbors a pixel has is found by doing a boxcar averaging of size $N_{size} \times N_{size}$ (typically $N_{size} = 7$) on the binary image. This smoothed array is thresholded-setting all pixels whose value is less than N_{live} to 0 and 1 otherwise.

Before processing actual linescan images, the prominent horizontal lines seen in many images (see Fig. 1 *A*) are removed to avoid being identified as potential Ca^{2+} sparks by the detection program. This is done by setting the zero frequency component (corresponding to time) of the image's Fourier transform to zero. The linescan image without horizontal lines is recovered by inverting the modified transform.

RESULTS

Confocal images of Ca^{2+} sparks

Fig. 1 *A* shows a linescan image of a rat ventricular cell obtained by using our homemade confocal microscope system (Parker et al., 1997). This system has a lateral FWHM of 0.31 μm and an axial FWHM of 0.41 μm. The bottom panel shows a simulated linescan in which both axial and lateral FWHM values were set to 0.35 μm. Setting the axial FWHM equal to the lateral FWHM greatly simplifies the analytic calculations without sacrificing much accuracy.

Before going to a quantitative description of the simulated Ca^{2+} sparks we point out two features of the simulated linescan. First, 1 *A* shows prominent horizontal lines that are spaced ~2 μm apart vertically; they originate on the t-tubules (Shacklock et al., 1995) and may arise from inhomogeneous distribution of dye. These lines are absent in the simulated image as we have assumed that the dyes, both mobile and immobile, are initially homogeneously distributed. Second, apart from the absence of the streaks, the simulated linescan image looks *qualitatively* like the linescan from an actual experiment.

Fig. 3 *A* illustrates how the simulated Ca^{2+} sparks are generated. The point source of Ca^{2+} release is assumed to be at the origin in panels *A–C*. The circles in the figure show the randomly chosen positions of the linescan in the *y–z* plane. Each circle corresponds to at least one Ca^{2+} spark (some positions may be chosen more than once) in the 200 linescan images made for this particular simulation. The triangles indicate the position of those Ca^{2+} sparks that were detected by the Ca^{2+} spark detection program. The arc encloses the region where 90% of the Ca^{2+} sparks were detected; the arc radius R_{90} is 0.56 μm. The linescan positions of Ca^{2+} sparks labeled *a* and *b* in Fig. 1 are correspondingly labeled in Fig. 3 *A*. As expected, the bright Ca^{2+} spark (*a*) arose when the linescan was near the point source and the dim Ca^{2+} spark (*b*) arose when the linescan was far away.

Performance of the Ca^{2+} spark detection program

As shown in Fig. 3 *A* a large number of Ca^{2+} sparks in the linescan images go undetected. The sensitivity of the program to pick out dim Ca^{2+} sparks can be altered by changing the detection parameters N_{size}, N_{live}, and $N_{generation}$. Decreasing N_{size} or N_{live} increases the sensitivity of the program allowing detection of dimmer Ca^{2+} sparks, but at the expense of making more false identifications. Increasing $N_{generation}$ has only a small effect on the sensitivity but reduces the number of false identifications. We could check the false identification rate because the positions of all Ca^{2+} sparks in the linescans were known. Note that falsely identified Ca^{2+} sparks were excluded from our measurements. The program parameters were adjusted empirically to achieve a balance between sensitivity and low false identification rate. We found that by using $N_{size} = 7$, $N_{live} = 12$, and $N_{generation} = 3$ the program identified all Ca^{2+} sparks correctly identified by observers and correctly identified dim Ca^{2+} sparks not identified by observers, while maintaining a false identification rate of ~2–5%. The number of dim Ca^{2+} sparks found by the program that was not detected by observers varied between observers but the program typically found ~50% more of the dimmest detectable Ca^{2+} sparks. The processing time for 100 linescan images,

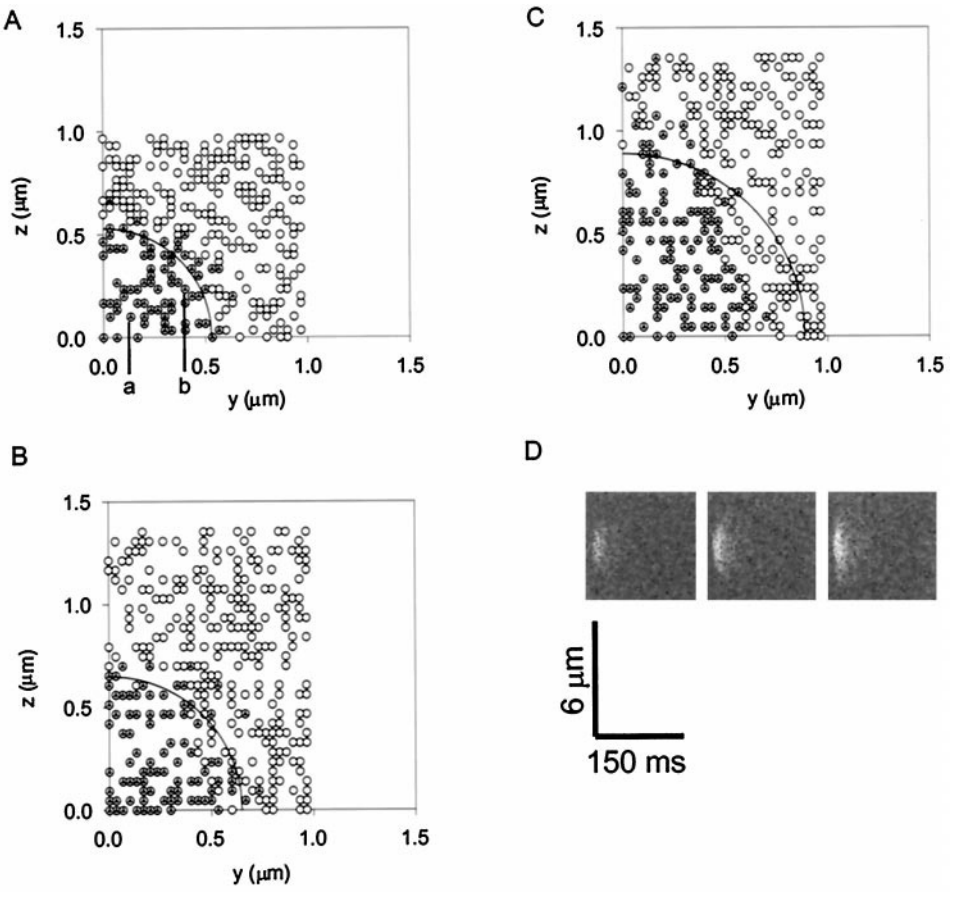

FIGURE 3 Spatial distribution of detected Ca^{2+} sparks as the microscope FWHM changes. In (*A*)–(*C*) the small circles mark the locations of the linescan in the *y*–*z* plane with respect to the source located at the origin. The triangles show the linescan positions at which the Ca^{2+} spark could be detected. The arc encloses the region where 90% of the detected Ca^{2+} sparks were found. In (*A*) the lateral and axial FWHM were $FWHM_{x,y} = FWHM_z = 0.35\ \mu m$. The detected Ca^{2+} sparks are symmetrically disposed about the origin as expected. The points marked *a* and *b* are the linescan positions that generated the similarly labeled Ca^{2+} sparks in Fig. 1 *B*. In (*B*), $FWHM_{x,y} = 0.2\ \mu m$ and $FWHM_z = 0.6\ \mu m$. Although $FWHM_z$ is three times as large as $FWHM_{x,y}$ the linescan positions of detected Ca^{2+} sparks are still symmetrically arrayed about the origin. In (*C*), $FWHM_{x,y} = 0.2\ \mu m$ and $FWHM_z$ is six times as large. The linescan positions of detected Ca^{2+} sparks are no longer symmetric about the origin, but show an elliptical pattern. In the absence of noise, all Ca^{2+} sparks are detected by the spark detection program. (*D*) shows the contrast increase of a Ca^{2+} spark as the axial FWHM decreases from 1.2 to 0.6 to 0.2 μm while keeping the lateral FWHM fixed to 0.2 μm.

166 pixels (500 ms) by 256 pixels (25.6 μm) in size, is ~2 min on an IBM RS-6000 workstation.

Properties of simulated Ca^{2+} sparks

Ca^{2+} sparks shown in Fig. 1 *B* were generated using a channel current of 1.4 pA, a channel open time of 10 ms (Rousseau and Meissner, 1989; Lukyanenko et al., 1996) with $\beta = 5$. We also ran an identical simulation except with $\beta = 2$. Ca^{2+} spark characteristics from both simulations are shown in Table 1.

The time for the fluorescence (that is, $G_i + G_m$) to decrease from peak value (measured at the brightest point of the Ca^{2+} spark) to half its value to the baseline is $t_{1/2}$. The peak ratio, or Ca^{2+} spark amplitude *a*, equals F/Fo where F is the peak fluorescence value and Fo is the baseline fluorescence value. The mean Ca^{2+} spark amplitude is given by $\langle F/Fo \rangle$ and the maximum ratio [occurring when $(y, z) = (0, 0)$] is F/Fo(max). The spatial spread of the Ca^{2+} spark at the time of the peak fluorescence is characterized by the FWHM. Because of the large variation in $t_{1/2}$ and FWHM, we also calculated these values [$t_{1/2}$(bright), FWHM(bright)] using only the 10 brightest Ca^{2+} sparks.

Typical $t_{1/2}$ values for Ca^{2+} sparks from heart cells is ~20 ms (Cheng et al., 1993), which is close to that found when $\beta = 5$ but not when $\beta = 2$. Note that the standard deviations are quite large, about half the mean $t_{1/2}$ value. The reason for this large variation is shown in Fig. 4 *A* where $t_{1/2}$ is plotted against the Ca^{2+} spark amplitude. The variation in $t_{1/2}$ is fairly small for the large amplitude Ca^{2+} sparks but is large for the low amplitude Ca^{2+} sparks because of noise.

Fig. 4 *B* shows a plot of $t_{1/2}$ against amplitude for the same set of simulations in Fig. 4 *A* but in the absence of noise. Since the Ca^{2+} sparks were generated identically, amplitude variations are due solely to variations in distance between linescan and Ca^{2+} spark origin. The decay time of identically generated Ca^{2+} sparks is controlled by the dif-

TABLE 1 Properties of simulated Ca^{2+} sparks

β	$t_{1/2}$ (ms)	$\langle F/Fo \rangle$	F/Fo(max)	FWHM (μm)	$t_{1/2}$(bright)	FWHM(bright)
2	12.3 ± 5.3	1.63 ± 0.37	3.18	1.83 ± 1.01	9.3 ± 1.7	2.08 ± 0.71
5	18.2 ± 9.9	1.62 ± 0.39	3.06	1.38 ± 0.90	14.4 ± 3.1	1.98 ± 0.62

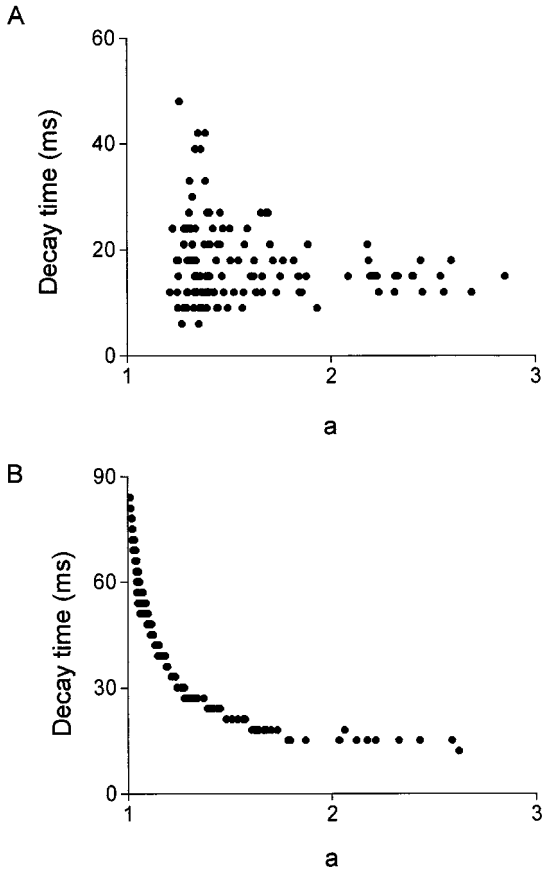

FIGURE 4 Plots of Ca^{2+} spark decay time ($t_{1/2}$) as a function of Ca^{2+} spark amplitude. Ca^{2+} sparks in simulated linescan images were identified with the Ca^{2+} spark detection program. All Ca^{2+} sparks were generated identically, so Ca^{2+} spark amplitude simply reflects distance between linescan and source. Thus decay time should reflect diffusion time within the sample volume and rise monotonically as the Ca^{2+} spark amplitude decreases, as shown in (*B*) obtained from noise-free linescans. The upward trend of decay time for decreasing amplitude is still evident when noise is present (*A*) but there is tremendous variability in the decay times when the Ca^{2+} spark amplitude is small.

fusion of Ca^{2+} into the scanned volume, so it increases with distance and, equivalently, decreases with Ca^{2+} spark amplitude. Viewed in isolation, Fig. 4 *B* suggests that the decay time could be used to distinguish whether a Ca^{2+} spark has a small amplitude because the linescan was far from the source or because the source strength was small. The results in Fig. 4 *A* cautions against such a method as virtually any decay time may be obtained for small amplitude Ca^{2+} sparks.

The mean Ca^{2+} spark amplitude is almost identical for $\beta = 2$ and 5 and is typical for experimentally measured Ca^{2+} sparks. F/Fo(max) values are also similar for the two values of β, indicating that despite the larger amount of dye available when $\beta = 5$ the amount of Ca^{2+} released is sufficient to saturate the dye.

The FWHM values for the 10 brightest Ca^{2+} sparks is $\sim$2 μm, which is about half the value reported by Gómez et al. (1996) for rat ventricular cells. Simulations carried out with longer open times or larger channel currents did not greatly alter the FWHM values.

Effect of changing microscope's FWHM

The triangles in Fig. 3 *A* showing the linescan positions at which the Ca^{2+} spark could be detected are symmetrically distributed around the origin, as expected since the axial and lateral FWHM values are equal. To study how this distribution changes when the blurring kernel is asymmetric, we increased the σ_z/σ_{xy} ratio to 3 (Fig. 3 *B*) and 6 (Fig. 3 *C*) where σ_{xy} was fixed to 0.2 μm. Note that the confocal parameters are different from those used to generate Fig. 3 *A*. The case where $\sigma_z/\sigma_{xy} = 1$ is not shown since the distribution of detected Ca^{2+} sparks is symmetric, as in Fig. 3 *A*. (Fig. 3, *A–C* may be interpreted in two equivalent ways: the point source is at the origin and the circles represent the linescan positions, or the linescan is fixed at the origin and the circles mark the point source locations. We take the latter viewpoint now so we can talk about the distribution of detected Ca^{2+} sparks instead of the more unwieldy distribution of linescan positions at which the Ca^{2+} spark was detected.) Fig. 3 *B* shows, surprisingly, that the distribution of detected Ca^{2+} sparks is still symmetric about the origin despite the axial FWHM being 3 times larger than the lateral FWHM. The distribution of detected Ca^{2+} sparks becomes asymmetric, however, when $\sigma_z/\sigma_{xy} = 6$, as shown in Fig. 3 *C*.

We were initially surprised to see the distribution in Fig. 3 *B* because we had expected to see an ellipsoidal distribution that parallels the elongation of the PSF along the *z*-axis. With increases in the depth of field (increasing σ_z) comes a loss in contrast of the Ca^{2+} spark, making it more difficult to detect the Ca^{2+} spark. This decrease in contrast with increases in σ_z is shown in Fig. 3 *D* (right to left) where the same Ca^{2+} spark is imaged with σ_z equaling 0.2, 0.6, and 1.2 μm, respectively. (No microscope to date has achieved an axial resolution of $\sim$0.2 μm, but we have used this value for illustration.) The F/Fo values for these three cases are 2.19, 2.64, and 3.12 (left to right) yielding Ca^{2+} concentration values of 312, 447, and 664 nM (Cheng et al., 1993). Thus the simple act of opening the confocal pinhole, which increases both axial and lateral FWHM, can reduce the Ca^{2+} concentration estimates.

The physical reason for the decrease in contrast as σ_z increases is that because the light energy is spread over a larger volume, the intensity must be lower to maintain energy conservation. Mathematically, this constraint is expressed in the larger denominator ($\sim\sigma_z$) in the normalization factor of the Gaussian kernel in Eq. 11.

Ca^{2+} spark amplitude distribution

Ca^{2+} spark amplitude distributions obtained from simulated linescan images are shown in Fig. 5. All Ca^{2+} sparks were generated with a channel current of 1.4 pA and channel open time of 10 ms; only the linescan positions were varied randomly. In the absence of noise, panel *A*, the Ca^{2+} spark amplitude distribution decreases monotonically except for statistical sampling variations. [Nonmonotonicity in the Ca^{2+} spark amplitude distribution due to sampling variation

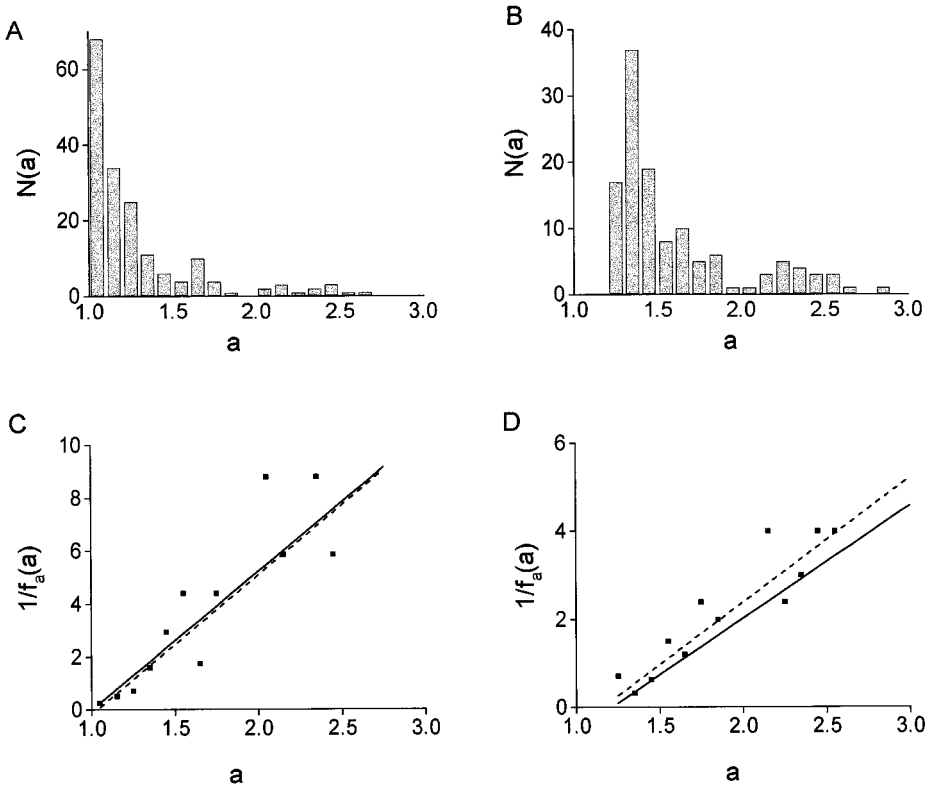

FIGURE 5 Amplitude histograms and $1/f_a(a)$ obtained using Ca^{2+} sparks in simulated linescan images identified by the Ca^{2+} spark detection program. (*A*) shows the Ca^{2+} spark amplitude distribution obtained from noise-free linescan images. All 176 Ca^{2+} sparks were detected by the Ca^{2+} spark detection program without false positives. (*C*) shows the plot of $1/f_a(a)$ (*squares*) calculated using the bin values in (*A*). The theoretical line (*solid*) is virtually identical to the best-fit line (*dashed*). In (*B*) noise was added to the linescan images so the very dim Ca^{2+} sparks were not detected. (*D*) shows the $1/f_a(a)$ values calculated from the bin values in (*B*) (*squares*); solid and dashed lines are as in (*C*). The maximum amplitude occurs when the confocal linescan goes through the spark origin. In noise-free images (*A*), $a_{max} = 2.62$ while in noisy images (*B*), $a_{max} = 2.85$.

can be distinguished from intrinsically multimodal distributions (for example when the SR Ca^{2+} release channels are arranged on a lattice, see below) by increasing the sample size or by changing the seed value of the random number generator. Intrinsically multimodal Ca^{2+} spark amplitude distributions are unaffected by these changes.]

These graphs illustrate the inherent difficulty in assessing the source strength distribution. Although all Ca^{2+} sparks in the linescan images were generated identically, because of the arbitrary placement of the linescan relative to the source, there is a broad distribution of measured Ca^{2+} spark amplitudes instead of a single narrow bin or narrow Gaussian distribution. A Gaussian distribution has been interpreted to indicate that Ca^{2+} sparks have stereotypic origins. However, Fig. 5 shows that, in our model, Ca^{2+} sparks generated identically do not generate a narrow Ca^{2+} spark amplitude distribution. This result is similar to that obtained by Pratusevich and Balke (1996).

One way that a monotonically decreasing Ca^{2+} spark amplitude distribution, Fig. 5 *A*, might be transformed into a Gaussian-like distribution is suggested by Fig. 5 *B*. In the presence of noise, Ca^{2+} sparks whose amplitude was $<\sim 1.2$ were not detected by the detection program. Moreover, more Ca^{2+} sparks whose amplitudes were in the range 1.3–1.4 were detected than those Ca^{2+} sparks with amplitudes of 1.2–1.3. When noise is present the Ca^{2+} sparks of low amplitude are not *detected* with the same reliability as the large amplitude Ca^{2+} sparks. Thus, although there were actually more low amplitude Ca^{2+} sparks in the linescan images (Fig. 1 *B*) these Ca^{2+} sparks are masked by noise and *appear* to occur less frequently. The difference in reliability is quantified by a visibility function proposed by Pratusevich and Balke (1996). The sigmoidal visibility function gives the probability of detecting a Ca^{2+} spark of a given amplitude and ranges from 0 for amplitudes near 1 and rises to unity as the Ca^{2+} spark amplitude increases. The Ca^{2+} spark amplitude distribution that is measured is then the product of the "ideal" amplitude distribution, obtained by a perfect detector in the absence of noise (Fig. 5 *A*), and the visibility function. Multiplying an appropriately shaped visibility function with an amplitude distribution such as in Fig. 5 *A* can give a Ca^{2+} spark amplitude distribution that is Gaussian-like and similar to those reported in the literature (Klein et al., 1996; Shorofsky et al., 1996, 1997; Shirokova and Ríos, 1997; Xiao et al., 1997; Wier et al., 1997).

The key question is whether the *intrinsic* properties of the SR Ca^{2+} release channel, not detector characteristics, produce these experimentally measured Ca^{2+} spark amplitude distributions. To answer this question we need to establish the relationship between the Ca^{2+} spark amplitude distribution and the underlying source strength distribution.

Relationship between the Ca^{2+} spark amplitude distribution and source strength distribution

Let $f_a(a)$ be the probability density function (pdf) of Ca^{2+} spark amplitudes. That is, the probability of finding a Ca^{2+} spark whose amplitude is between $a - \delta a/2$ and $a + \delta a/2$

is $f_a(a)\delta a$. Likewise, let $f_\alpha(\alpha)$ be the pdf of the source strength. The source strength α may refer to the SR Ca^{2+} release channel current for a fixed channel open time or to the open time for a fixed channel current.

To establish the link between f_a and f_α consider a simple and intuitive example. Suppose that a light bulb located at the origin flashes with intensity α' with probability $p(\alpha')$ and flashes with intensity α'' with probability $p(\alpha'') = 1 - p(\alpha')$. The light intensity a that an observer measures depends on his/her distance r from the lamp and the lamp intensity α, and is given by the *observation function*, $g(\alpha, r)$

$$a = g(\alpha, r). \tag{13}$$

Suppose when the observer is at r' the lamp flashes with intensity α' and the observer measures intensity $a_1 = g(r', \alpha')$. If the observer moves randomly then the mean number of times that he/she measures an intensity a_1 is proportional to the probability of being at a distance r', $p(r')$, times the probability that the lamp flashed with intensity α', that is

$$p_a(a_1) \sim p_r(r')p_\alpha(\alpha'). \tag{14}$$

The observer will also measure intensity a_1 when the lamp flashes with intensity α'' and his/her distance r'' is adjusted accordingly to give $a_1 = g(r'', \alpha'')$. The appropriate distance is given by

$$r'' = \rho(\alpha'', a_1).$$

The function $\rho(a, \alpha)$ can always be found provided the observation function $g(\alpha, r)$ is a strictly monotonic function of r. Thus the probability p_a of measuring intensity a_1 becomes

$$p_a(a_1) = p_r(r')p_\alpha(\alpha') + p_r(r'')p_\alpha(\alpha''). \tag{15}$$

To extend the argument to a continuum of source strengths let $F_a(a)$ be the probability that the measured Ca^{2+} spark amplitude $g(\alpha, r) < a$. $F_a(a)$ is the cumulative distribution function

$$F_a[g(\alpha, r) < a] = \int_{\alpha'} \int_{r'} f_\alpha(\alpha')f_r(r')dr'd\alpha', \tag{16}$$

where $f_r(r)$ is the pdf of being at a distance r from the origin.

Although α and r are independent random variables, the values of α and a constrain the lower limit of integration of r. In order to satisfy $g(\alpha, r) < a$, the lower bound of r must be $\rho(\alpha, a)$. Thus,

$$F_a[g(\alpha, r) < a] = \int_{\alpha'} \int_{\rho(\alpha', a)}^{R} f_\alpha(\alpha')f_r(r')d\alpha'dr'. \tag{17}$$

The largest α compatible with a given a is given by $\alpha_{max} = g^{-1}(a, r)$. Thus Eq. 17 becomes

$$F_a(a) = \int_0^{g^{-1}(a,R)} \int_{\rho(\alpha', a)}^{R} f_\alpha(\alpha')f_r(r')d\alpha'dr'. \tag{18}$$

Differentiating $F_a(a)$ yields the probability density function $f_a(a)$

$$f_a(a) = -\int_0^{g^{-1}(a,R)} f_\alpha(\alpha')f_r[\rho(\alpha', a)]\frac{\partial \rho}{\partial a}(\alpha', a)d\alpha'. \tag{19}$$

This integral equation relating $f_a(a)$ to $f_\alpha(\alpha)$ is the main result. We now need to find specific forms of f_α, f_r, and ρ. If the linescan can be at any position between $0 \le r \le R$ with equal probability, then $f_r(r) = 2r/R^2$. Note that the use of r and not (y, z) comes from the implicit assumption that the blurring along the lateral dimensions x and y is the same as along the z-axis. Another assumption implicit in the use of r is that the diffusion is radially symmetric.

Explicit form for the observation function $g(\alpha, r)$

Because of the nonlinear buffer reactions, the observation function cannot be found analytically. We determined $g(\alpha, r)$ empirically using the following procedure. Linescan images (100–200) containing a total of ~150–300 Ca^{2+} sparks were generated with a set of parameters for the reaction-diffusion simulations and a channel current of α, say 1.4 pA, and a fixed channel open time (10 ms). Ca^{2+} sparks were found using the Ca^{2+} spark detection program and their amplitudes (a = F/Fo) calculated. Since the (y, z) coordinates of each linescan were known, the amplitude at the distance $r = (y^2 + z^2)^{1/2}$ could be calculated. The pairs of (a, r) were fit to the function

$$a = g(\alpha, r) = A(\alpha)\exp[-C(\alpha)^2r^2] + B(\alpha). \tag{20}$$

This procedure was repeated for different channel currents to determine $A(\alpha)$, $B(\alpha)$, and $C(\alpha)$.

The observation functions for four different channel currents are shown in Fig. 6 *A*. The solid curve shows the best fit to the data and, for clarity, data points are only shown for $\alpha = 0.7$ pA and $\alpha = 2.8$ pA. $A(\alpha)$ was fit to the hyperbolic function

$$A(\alpha) = 3.75\alpha/(2.06 + \alpha) \tag{21}$$

and $C(\alpha)$ to the line

$$C(\alpha) = 3.32 - 0.33\alpha \tag{22}$$

shown in Figs. 6 *B* and 6 *C*. No theoretical significance is attached to the specific forms of $A(\alpha)$ and $C(\alpha)$; they were simply chosen for simplicity. $B(\alpha)$ was essentially independent of α varying between 1.20 and 1.25. This is expected since B should only reflect the sensitivity of the detection program and the amount of added noise. Moderate (3–5-fold) reduction of k_m^+, k_m^-, k_i^+, and k_i^- values did not affect

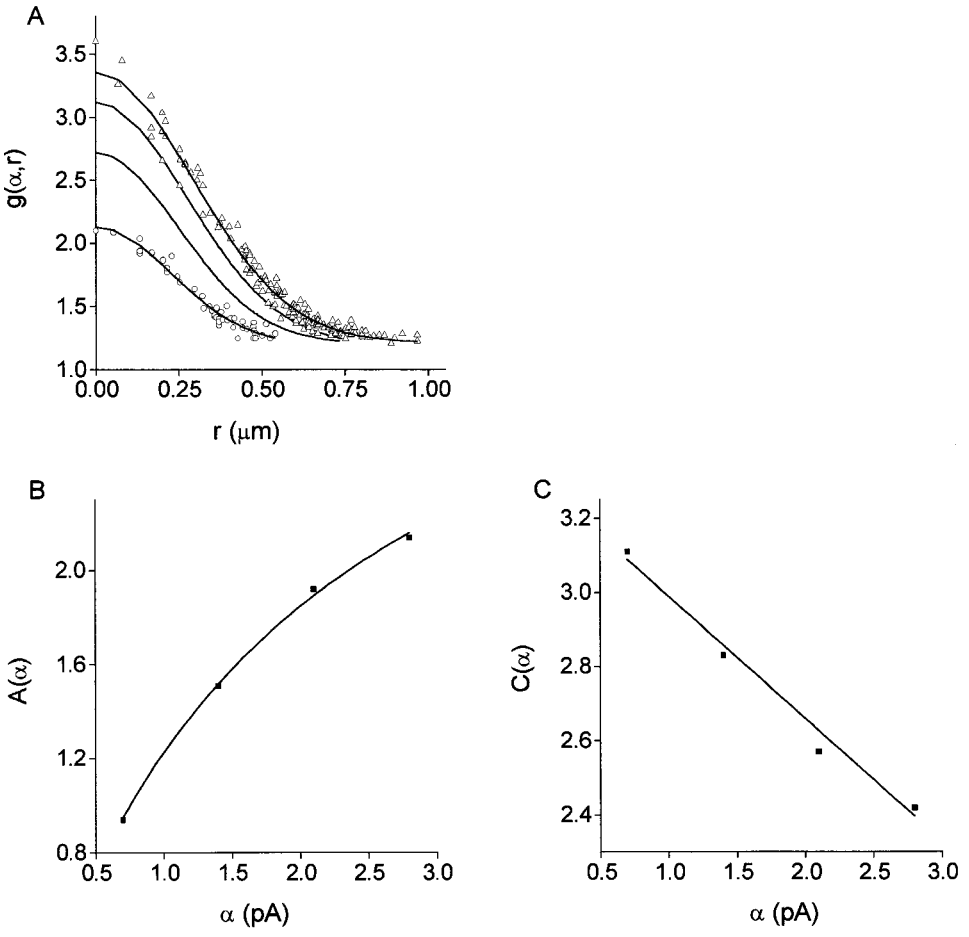

FIGURE 6 Determining the observation function for variable channel current. Ca^{2+} sparks from simulated linescan images were identified with the Ca^{2+} spark detection program. (*A*) shows the measured amplitude as a function of distance between the linescan and source for each identified Ca^{2+} spark (*symbols*). The data points were fit to the function $A(\alpha)\exp\{-[C(\alpha)r]^2\} + B(\alpha)$, where α is the channel current. For clarity only the data points for $\alpha = 0.7$ (*circles*) and 2.8 (*triangles*) pA are shown. Intermediate curves are for $\alpha = 1.4$ and 2.1 pA. (*B*) and (*C*) show the fit parameters $A(\alpha)$ and $C(\alpha)$ from (*A*) as functions of α.

the functional form of the observation function or of $A(\alpha)$ and $C(\alpha)$.

In the next section we will derive a specific relationship between f_α and f_a that will allow us to examine the effects that different source strength distributions have on the Ca^{2+} spark amplitude distribution. The specific relationship between f_α and f_a depends, of course, on our assumption that the observation function is Gaussian. Different observation functions yield different relationships between f_α and f_a. Thus, it is worthwhile to examine the range of conditions under which the observation function is likely to be Gaussian. When Ca^{2+} release comes from a point source and the source strength is sufficiently weak so that the dye does not saturate, then the Ca^{2+} bound fluo-3 distribution is approximately Gaussian. We assumed that the PSF is Gaussian, which well approximates the actual PSF for a correctly aligned confocal microscope with a fairly small pinhole. The convolution of the Gaussian Ca^{2+} bound fluo-3 concentration profile with the Gaussian PSF gives a Gaussian image; the observation function is the profile of this convolution. We note that the spatial profiles of many Ca^{2+} sparks are approximately Gaussian (Parker et al., 1996; Gómez et al., 1996).

The observation function will deviate from a Gaussian when the source is extended [see Smith et al. (1998) for a discussion of extended sources], when the dye is saturated, or the confocal microscope is poorly aligned. Under these conditions the observation function must be amended. Later we will see the effect of dye saturation on f_a.

Explicit relationship between f_α and f_a

From Eq. 20 it follows that $\rho(a, r)$ is given by

$$\rho(\alpha, a) = \frac{1}{C(\alpha)}\left(\log\frac{A(\alpha)}{a - B(\alpha)}\right)^{1/2} \tag{23}$$

and

$$\frac{\partial\rho}{\partial a}(\alpha, a) = \frac{-1}{2C(\alpha)}\left(\log\frac{A(\alpha)}{a - B(\alpha)}\right)^{-1/2}\frac{1}{a - B(\alpha)}. \tag{24}$$

Now suppose that all Ca^{2+} sparks are generated identically; that is, there are no variations in the source strength then the source strength pdf is $f_\alpha(\alpha) = \delta(\alpha - \alpha_o)$, where δ is the Dirac delta-function. In this case Eq. 19 becomes

$$f_a(a) = -f_r[\rho(\alpha_o, a)]\frac{\partial\rho}{\partial a}(\alpha_o, a). \tag{25}$$

The smallest amplitude that can be attained with this α is $a_{min}(\alpha_o) = g(\alpha_o, R)$ and the largest is $a_{max}(\alpha_o) = g(\alpha_o, 0)$. Using Eqs. 23, 24, and $f_r(\rho) = 2\rho/R^2$, the explicit expression for $f_a(a)$ in Eq. 25 is

$$f_a(a) = \frac{1}{C(\alpha)^2 R^2 (a - B)} \cdot \{H[a - a_{min}(\alpha_o)] - H[a - a_{max}(\alpha_o)]\}. \quad (26)$$

The difference of the Heaviside functions, H, limits $f_a(a)$ to $a_{min} < a < a_{max}$. [The Heaviside function $H(a - x)$ is a step function that equals 1 for $x \geq a$ and 0 otherwise.] Between these limits $f_a(a) \sim (a - B)^{-1}$.

Equation 26 is one of the key results of this paper. It implies that if all Ca^{2+} sparks were generated identically and if the observation function were Gaussian (Eq. 20), then the resulting Ca^{2+} spark amplitude histogram as measured by confocal microscopy should be hyperbolic, not Gaussian. Accordingly, a plot of $1/f_a(a)$ against a yields a straight line.

Relationship between f_a and the Ca^{2+} spark amplitude histogram $N(a)$

Let $N(a)$ be the number of Ca^{2+} sparks having amplitudes between $a - \Delta/2 \leq a \leq a + \Delta/2$, where Δ is the binwidth. Then

$$N(a) = N_{total} \int_{a-\Delta/2}^{a+\Delta/2} f_a(a')da' \approx N_{total} \Delta f_a(a), \quad (27)$$

where N_{total} is the total number of Ca^{2+} sparks. Equation 27 can be turned around to get an estimate of f_a, f_a^{est},

$$f_a^{est} = N(a)/(N_{total} \cdot \Delta). \quad (28)$$

We can now compare the theoretical curve $f_a(a)$ given by Eq. 26 to that given by Eq. 28. In Fig. 5 *C* we have plotted $1/f_a(a) = N_{total}\Delta/N(a)$ (*squares*), where $N(a)$ is the data from Fig. 5 *A*, $N_{total} = 176$ Ca^{2+} sparks, and $\Delta = 0.1$. The solid line is the theoretical f_a calculated using Eq. 26 with $C(\alpha = 1.4) = 2.86$ and $R = R_{90} = 0.80$ μm; this line is the best descriptor of the data points as it is virtually coincident with the best fit line (*dashed line*). This agreement between simulation and theoretical results is important because it provides a check on the derivation of the relationship between f_a and f_α. Thus we can simulate the distribution of Ca^{2+} spark amplitudes in a new way. Instead of making linescan images, detecting the Ca^{2+} sparks, and then calculating their amplitudes, we used the following method. The confocal linescan position was chosen randomly in the y–z plane and its distance r from the Ca^{2+} spark at the origin was calculated. The amplitude was then calculated using the observation function. With this new method we could simulate conditions that would be extremely tedious or impossible by the old method.

Estimating α from the Ca^{2+} spark amplitude histogram

In this instance α was known so the theoretical line could be calculated. In practice α is unknown but can be calculated from the information available in the Ca^{2+} spark amplitude histogram as follows. If the plot $1/N(a)$ against a falls on a single straight line then the data are consistent with a delta-function source strength pdf, $\delta(\alpha - \alpha_o)$. (See below for f_a when f_α is more complicated than a single delta-function.) α_o is calculated using the largest measured Ca^{2+} spark amplitude using Eqs. 20 (with $r = 0$) and 21. In this case $a_{max} = 2.85$, which gives $\alpha_o = 2.0$, precisely the value used in the simulations. Having calculated α_o, R can be calculated for each a using Eqs. 22 and 20. The calculated values will naturally depend on the simulation parameters such as the amount of buffer available and their kinetics of reaction with Ca^{2+}.

f_a of more complicated f_α

Suppose instead of f_α being a single Dirac δ-function, f_α is the weighted sum of δ-functions

$$f_\alpha(\alpha) = \sum_i \sigma_i \delta(\alpha - \alpha_i) \quad (29)$$

where σ_i gives the probability of the source strength being α_i so the σ values satisfy $\Sigma_i \sigma_i = 1$. Since Eq. 26 holds for all α it follows that

$$f_a(a) = \sum_i \frac{\sigma_i}{C(\alpha_i)^2 R^2 (a - B)} \cdot \{H[a - a_{min}(\alpha_i)] - H[a - a_{max}(\alpha_i)]\}. \quad (30)$$

Since $a_{min}(\alpha)$ and $a_{max}(\alpha)$ are increasing functions of α, f_a is the sum of terms $(a - B)^{-1}$ that are progressively shifted to the right as α increases. Because of this shifting, $f_a(a)$ will not behave as $(a - B)^{-1}$. A plot of $1/f_a(a)$ against a shows jump discontinuities and slope changes at $a_{max}(\alpha_i)$.

To illustrate the last point, we simulated the case where there were two populations of channels passing either 1 or 2 pA, with a fixed channel open time of 10 ms, and opening with equal probability. The source strength pdf is, in this case, $f_\alpha(\alpha) = 0.5\delta(\alpha - 1) + 0.5\delta(\alpha - 2)$. We simulated the measurement of 1500 Ca^{2+} sparks in which all Ca^{2+} sparks having amplitude >1.05, but no others, were detected. The amplitude histogram for this simulation is shown in Fig. 7 *A*. As in Fig. 5 *A*, the amplitude histogram decreases monotonically for the most part. (There is less sampling variation than in Fig. 5 *A* because the number of Ca^{2+} sparks is about eight times larger in Fig. 7 *A*.) There is nothing strikingly different between the two histograms that would suggest the presence of two populations of channels. The plots of $\Delta N_{total}/N(a)$ against a shown in Figs. 5 *C* and 7 *C*, however,

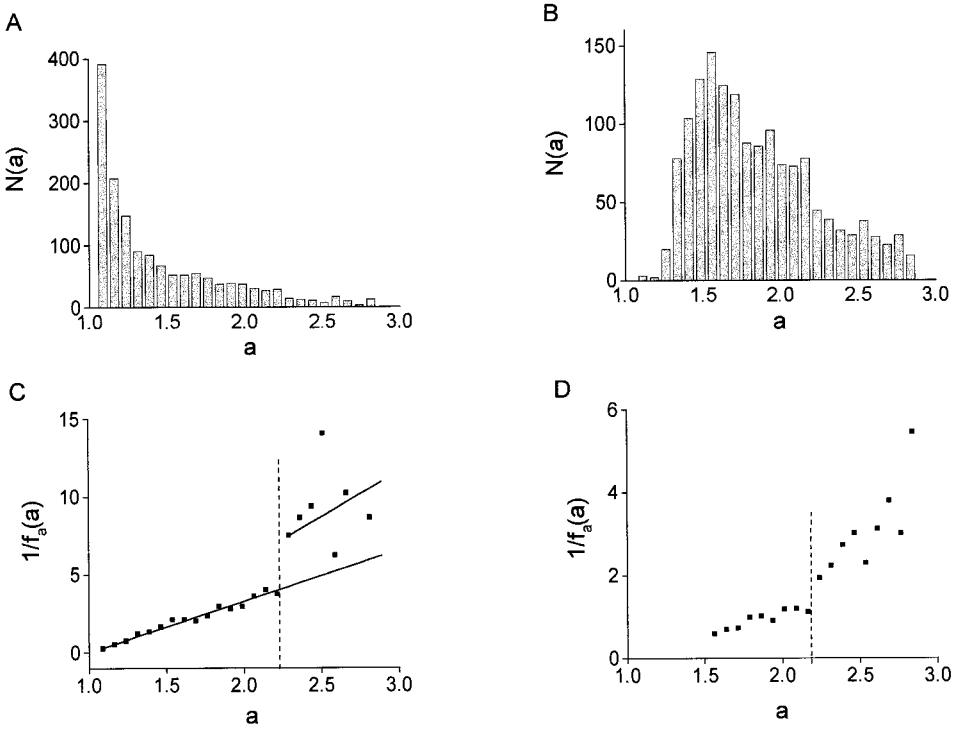

FIGURE 7 Amplitude distribution and $1/f_a(a)$ when f_α is the sum of two Dirac delta-functions $f_\alpha(\alpha) = \delta(\alpha - 1\text{ pA})/2 + \delta(\alpha - 2\text{ pA})/2$. (*A*) results from measuring all Ca^{2+} sparks whose amplitudes are >1.05. In (*B*) the probability of detecting a Ca^{2+} spark of amplitude a was determined by the value of the sigmoidal visibility function $\psi(a)$. (*C*) is the plot of $1/f_a(a)$. The solid lines show the theoretical distribution and the squares are $1/f_a^{est}$ calculated from the histogram in (*A*). The jump discontinuity, marked by the dotted line, occurs at $a_{max}(\alpha = 1)$, which is the largest amplitude Ca^{2+} spark that the $\alpha = 1$ pA source can generate. (*D*) shows $1/f_a^{est}$ calculated from the histogram in (*B*). Only values from the descending portion of the histogram (>1.5) were used. The slopes of the points are shallower than the theoretical values but the jump discontinuity occurs at the same place.

clearly show a qualitative difference between the Ca^{2+} spark amplitude distributions of Fig. 5 *A* and 7 *A*. The jump discontinuity occurs at $a(\alpha = 1)_{max} = A(\alpha = 1) + B = 2.23$, indicated by the dotted line.

To understand the physical origin of the jump discontinuity notice that the small amplitude Ca^{2+} sparks ($a < 2.23$) can arise from opening of either the $\alpha = 1$ pA channel or the larger $\alpha = 2$ pA channel. Thus the amplitude histogram for $a < 2.23$ reflects contributions from both channels. The Ca^{2+} spark amplitude of 2.23 arises when the linescan goes directly through the center of the $\alpha = 1$ pA source. Larger amplitude Ca^{2+} sparks ($a > 2.23$) can arise from only the $\alpha = 2$ pA channel. Thus the histogram suddenly loses contributions from the $\alpha = 1$ channel beyond $a = 2.23$, giving the jump discontinuity in the $1/f_a$ plot.

The solid lines are the theoretical values of $1/f_a(a)$ computed using (30). The slope of the line for a between 1 and 2.23 equals $R^2[\sigma_1/C^2(\alpha = 1) + \sigma_2/C^2(\alpha = 2)]^{-1} = 3.24$ where $R = R_{90} = 0.64$ μm. The slope of the line for a between 2.23 and $a(\alpha = 2)_{max} = 2.85$ is $2R^2C^2(\alpha = 2) = 5.80$.

Fig. 7 *B* shows the Ca^{2+} spark amplitude histogram obtained using the same simulation parameters in 7 *A*, but also incorporating a visibility function in our Ca^{2+} spark generation simulations. The sigmoidal visibility function is

$$\psi(a) = \frac{(a-1)^n}{(K-1)^n + (a-1)^n}, \qquad (31)$$

where $n = 6$ and $K = 1.4$. The visibility function worked as follows. For a given Ca^{2+} spark amplitude a, a random number between 0 and 1 from a uniform distribution was chosen. If the random number was less than $\psi(a)$ then the Ca^{2+} spark was detected and its amplitude measured; otherwise the Ca^{2+} spark was ignored.

The Ca^{2+} spark amplitude pdf is now $\psi(a)f_a(a)$. To estimate f_a, we used the section of the histogram from the peak ~1.5 and to the right. This section of the histogram contains $N_{total} = 1164$ Ca^{2+} sparks and the bin size is $\Delta = 0.075$. The plot of $N_{total}\Delta/N(a)$, shown in Fig. 7 *D*, shows a jump discontinuity and slope change at the expected value of $a(\alpha = 1)_{max} = 2.23$.

Extracting α values from the Ca^{2+} spark amplitude histogram

When the $1/N(a)$ vs. a plot shows a distinctive break, as in Fig. 7, *C* and *D*, this indicates a two-population distribution of source strengths. By using the largest measured amplitude a_{max}, 2.85 for the data in Fig. 6 *A* in Eq. 21 gives the larger $\alpha = \alpha_{big} = 2.0$ pA. The smaller $\alpha = \alpha_{small}$ is calculated using a at the jump discontinuity, which occurs between $2.21 \le a \le 2.29$. Using the average value of 2.25 gives $\alpha_{small} = 1.03$ pA.

To calculate the probabilities σ_1 and σ_2, we require the slopes of the two lines that are fitted to the points in the $1/f_a$ distribution to the left and to the right of the jump discontinuity. Let m_1 be the slope of the best fit line to the points before the jump discontinuity and m_2 the slope of the best fit line to the point right of the jump. Let $C_1 = C(\alpha_{small})$ and

$C_2 = C(\alpha_{big})$. The slopes of the $1/f_a$ distribution are given by Eq. 30 and satisfy the two equations

$$m_2 = \frac{R^2 C_2^2}{\sigma_2} \tag{32}$$

$$m_1 = \left(\frac{\sigma_1}{C_1^2} + \frac{\sigma_2}{C_2^2}\right)^{-1} \quad R^2 = \left(\frac{1-\sigma_2}{C_1^2} + \frac{\sigma_2}{C_2^2}\right)^{-1} R^2. \tag{33}$$

These two equations allow for solving for the two unknowns R and σ_2.

The slopes of the best fit lines for Fig. 7 *C* are $m_1 = 3.17$ and $m_2 = 4.23$; the theoretical values are 3.24 and 5.80, respectively. Using the best fit values gives $\sigma_1 = 0.3$ and $\sigma_2 = 0.7$; the actual values are $\sigma_1 = \sigma_2 = 0.5$. The main source of error is in the slope m_2, which is expected to be the least accurately known parameter since the number of points in each bin above the jump discontinuity is small, so scatter is magnified in the plot of $1/f_a$.

f_a when f_α is normally distributed

To allow for variation in the source strength we replaced the Dirac delta-function with a Gaussian distribution. Fig. 8 *A* shows the Ca^{2+} spark amplitude distribution when f_α is Gaussian with a mean of 1 pA and standard deviation of 0.1 pA. Panel *B* shows the $1/f_a^{est}$ (*squares*) and $1/f_a$ (*solid curve*), where f_a was calculated using Eq. 30. For comparison, panels *C* and *D* show the corresponding Ca^{2+} spark amplitude distribution and $1/f_a$ curves for $f_\alpha(\alpha) = \delta(\alpha - 1)$. The linear part of the $1/f_a$ curve in panel *B* (for *a* between 1 and ~2) has a slope of 2.7, which is close to 2.6, the slope of the line in panel *D*. The main difference between the $1/f_a$ curves is the upward sloping part in panel *B* that is absent from the curve in panel *D*. This upward slope indicates that the number of Ca^{2+} sparks with amplitude >2.1 decreases rapidly. This difference can be seen in the Ca^{2+} spark amplitude histograms: in panel *C* the histogram abruptly ends at 2.2, while the amplitude histogram extends slightly further out in panel *A*. The difference is subtle and would be difficult to distinguish between the two distributions based on $1/f_a^{est}$ given the scatter at large amplitudes. The error in assuming the Ca^{2+} spark amplitude distribution in panel *A* derives from a delta-function f_α is not great in this case. Using the maximum measured amplitude of 2.35, we calculate a source strength of 1.16 pA.

f_a when f_α is exponentially distributed

Up to now, α represented the channel current with the understanding that the channel open time was fixed. Now we fix the channel current to 1.4 pA and let α represent the channel open time (in ms). We determined the observation function, $g(\alpha, r)$, $A(\alpha)$, and $C(\alpha)$ for varying channel times in a similar manner described above. The observation function $g(\alpha, r)$ is the same as in Eq. 20 and A and C are now given by $A(\alpha) = 3.36\alpha/(12.16 + \alpha)$ and $C(\alpha) = 3.10 - 0.027\alpha$. In planar bilayer studies, SR Ca^{2+} release channels have an open time that is exponentially distributed (Rousseau and Meissner, 1989). Fig. 9 *A* shows the Ca^{2+} spark amplitude histogram when the channel open time was exponentially distributed with a mean open time of 5 ms. Fig. 9 *B* shows the $1/f_a$ curve, calculated using Eq. 30, and $1/f_a^{est}$.

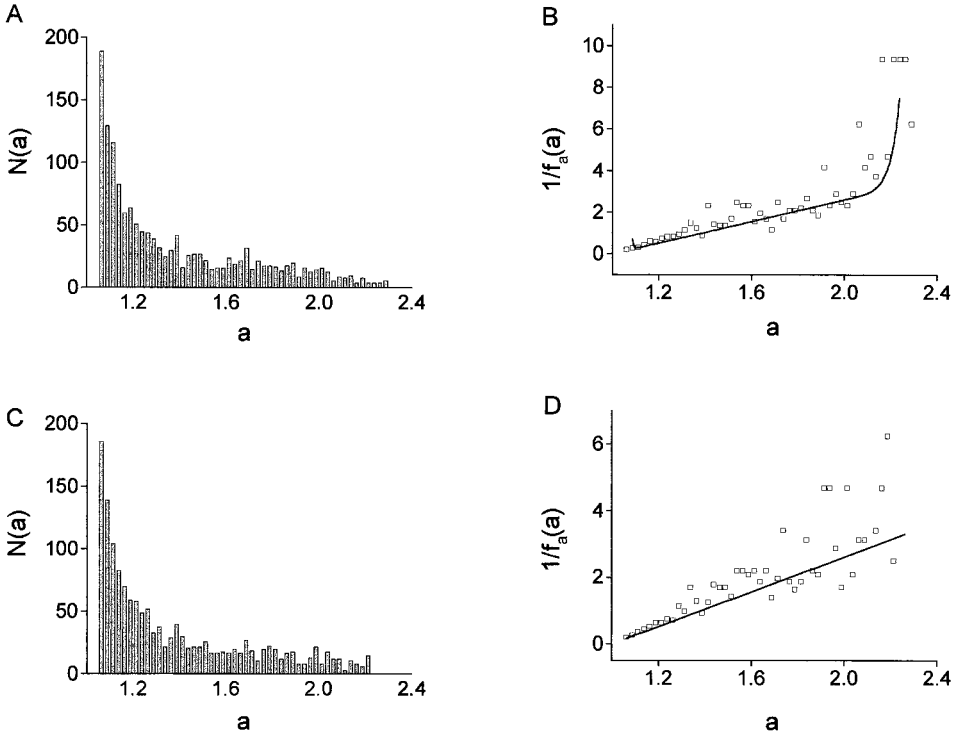

FIGURE 8 Amplitude distributions and $1/f_a(a)$ for Gaussian distribution of source amplitudes (*A* and *B*) and for a delta-function distribution of source amplitudes (*C* and *D*). The Gaussian source amplitude distribution had a mean of 1 pA and standard deviation of 0.1 pA; the delta-function distribution was centered at 1 pA.

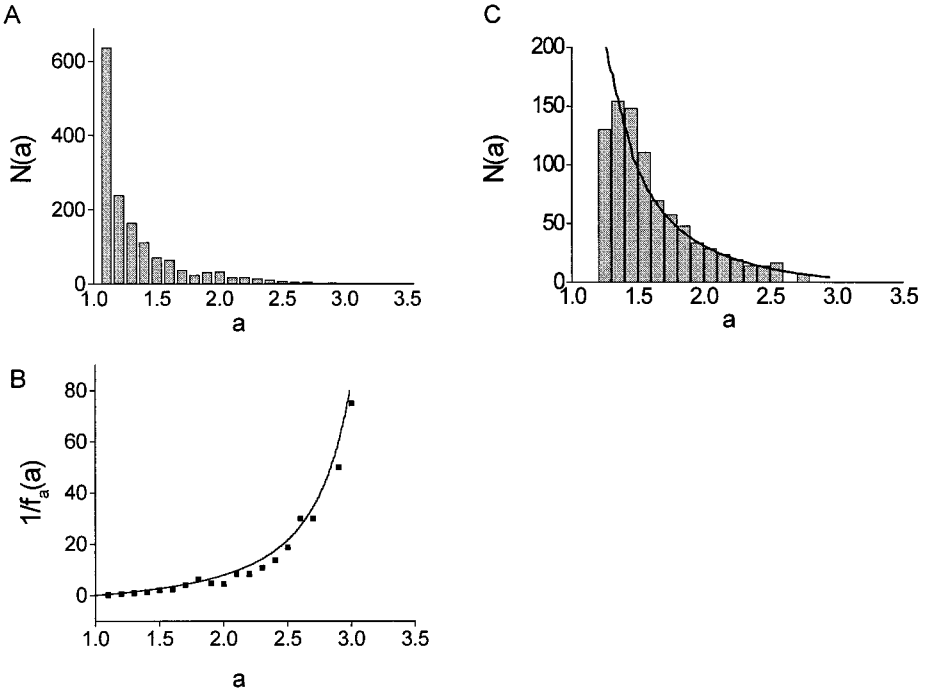

FIGURE 9 Amplitude distribution (*A*) and $1/f_a(a)$ (*B*) when channel open time is exponentially distributed. The mean open time was 5 ms and the channel current was fixed to 1.4 pA. Note the upward curvature of the $1/f_a$ graph even at small Ca^{2+} spark amplitudes, unlike those in previous figures that increased linearly. (*C*) Data from Fig. 1 *E* of Song et al. (1997) (*bars*) fitted to the model curve (*solid line*) generated using Eqs. 28 and 30 and assuming a 1.4 pA channel current, mean channel open time of 6 ms, and minimum detectable Ca^{2+} spark amplitude of $B = 1.2$.

In contrast to the $1/f_a$ curves in Figs. 5, 7, and 8 that increased linearly for small a, the $1/f_a$ curve in Fig. 9 *B* has an upward curvature.

Fig. 9 *C* shows a case where the model results were fit to actual experimental data. The data (*bars*), taken from Fig. 1 *E* of Song et al. (1997), show the amplitude distribution of Ca^{2+} sparks from rat ventricular cells. The $1/N(a)$ plot of their data was concave up, as in Fig. 9 *B*, hinting that the Ca^{2+} sparks were generated by channels whose open times were exponentially distributed. We could fit their data quite well (*solid line*) by assuming a channel current of 1.4 pA and the channel mean open time of 6 ms, the value found by Rousseau and Meissner (1989). This mean open time value is between the values of 1.02 ms and 17.82 ms measured by Xiao et al. (1997). If the Ca^{2+} sparks were derived from channels with two characteristic open times, we cannot distinguish them. Although we might obtain equally good fits using slightly different currents and correspondingly altered mean open times, we could not get a good fit by assuming a 2.8 pA channel current.

Spark amplitude distribution when sources are spatially distributed

We have been assuming that for a given linescan a Ca^{2+} spark from only a single source could be imaged. In heart cells, however, there is a spatial distribution of release sites that are spaced ~0.76 μm apart in the y–z plane (Parker et al., 1996). We therefore studied the effect that a spatial distribution of sources might have on the Ca^{2+} spark amplitude distribution. To do this we assumed that release sites were arranged in a periodic square lattice in the y–z plane. For each "cell" a linescan position, which defined the origin, was chosen. Sources at lattice sites within the circle of radius R (2 μm) centered at the origin were able to generate a Ca^{2+} spark. Each source has a 0.1 chance of releasing Ca^{2+} for each linescan and could be assigned a different channel current α.

For every linescan, each source within the circle was checked to see whether it was releasing Ca^{2+} and, if so, the Ca^{2+} spark amplitude was calculated using the observation function in Eq. 20 with A and C given by Eqs. 21 and 22. This procedure was repeated for each "cell."

We simulated the case where the source strength at each site was chosen from a normal distribution with a mean of 2 pA and standard deviation of 0.1 pA, and channel open time of 10 ms. The lattice spacing was set to 0.7 μm. Fig. 10 *A* shows the Ca^{2+} spark amplitude distribution obtained from 200 cells. There is no obvious qualitative difference between this histogram and that in Fig. 8 obtained when a linescan sampled a single site. This observation is supported by the similarity of the $1/f_a$ curve in Fig. 10 *B* to that in Fig. 8 *D*. The distance probability density function $f_r(r)$ shown in Fig. 10 *C* provides the answer for the similarities. f_r^{est} was calculated from the histogram of distances from the linescan to the sources using Eq. 28, *mutatis mutandis*. The line giving the best fit to the data has a slope of 0.49. Recall that if the linescan could be anywhere with respect to a *single source* then $f_r(r) = 2r/R^2$, which is linear in r and has a slope of $2/R^2$. For $R = 2$ μm, the slope is 0.5. Thus the spatial distribution of sources *appear* to behave as a single source.

The reason this is so is as follows. For a single cell there are only a few distinct distances between the linescan and the sources. But because for each cell the linescan is randomly placed, each cell contributes a different set of distances. Given a sufficient number of cells, the set of all

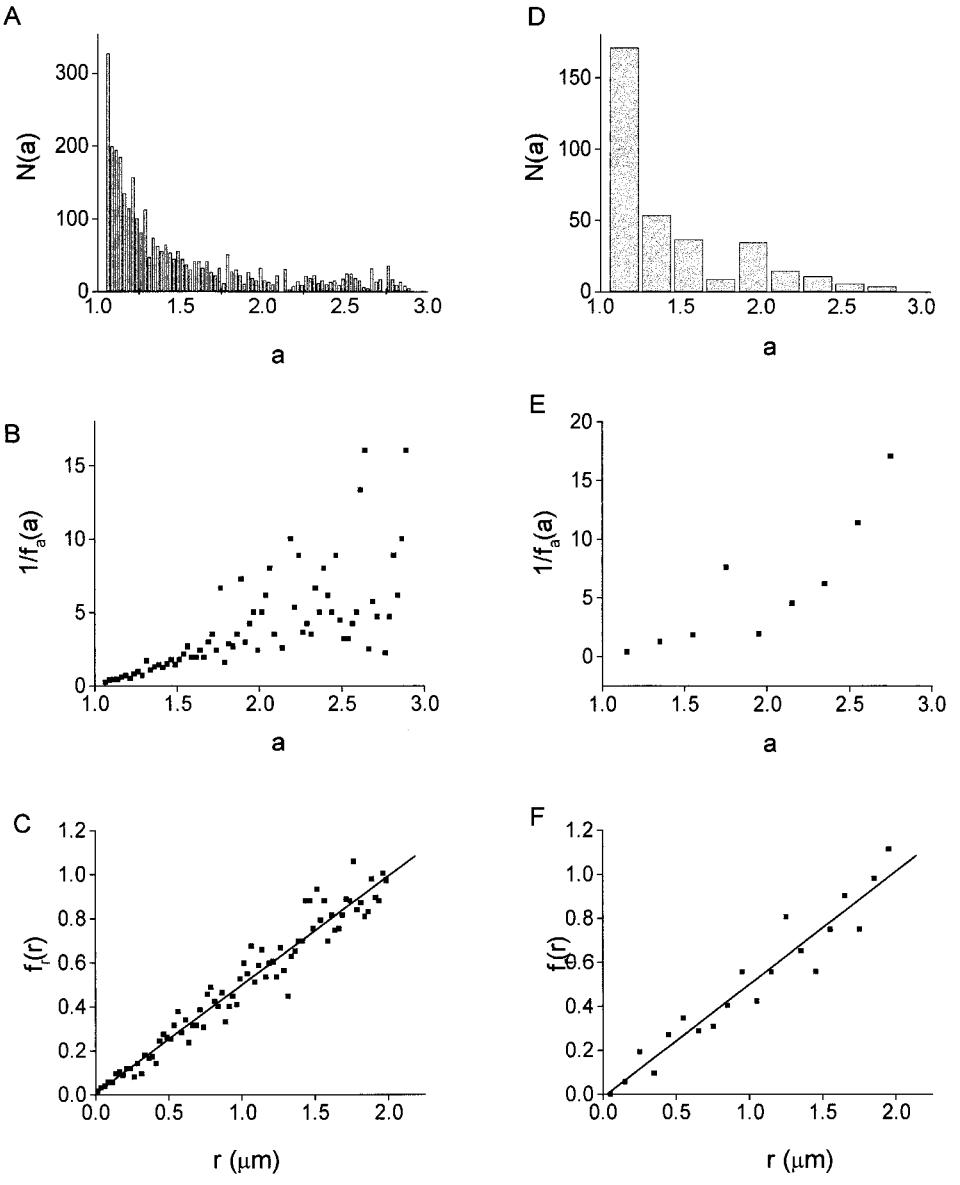

FIGURE 10 Effect of spatial distribution of sources on Ca^{2+} spark amplitude distribution. (*A*)–(*C*) were obtained using 200 "cells"; (*D*)–(*F*) were obtained using 20 cells. (*C*) and (*F*) show the pdf of the distance of the sources from the linescan. Both slopes are close to 0.5, indicating that the distribution of sources behave as a single source.

distances begin to uniformly cover the set of all possible distances, so $f_r^{est} \rightarrow 2r/R^2$. Since the distributed sites behave as a single source, the Ca^{2+} spark amplitude distribution in Fig. 10 *A* looks similar to that in Fig. 8 *A*.

Using this line of reasoning it follows that the lattice spacing has no effect on the Ca^{2+} spark amplitude distribution provided the Ca^{2+} sparks occur independently. This was confirmed by using a lattice spacing of 0.35 μm and getting essentially the same result. The slope of the best fit line to f_r was 0.50.

We repeated the simulations using 20 cells instead of 200, as shown in Fig. 10, *D*–*F*. The bin size in Fig. 10 *D* is larger that in Fig. 10 *A* because there are only 64 unique amplitude values. The slope of the line in Fig. 10 *F* has a slope of 0.51, nearly identical to the theoretical value of 0.5, showing that even with only 20 cells there is sufficient randomization to make the distribution of sources appear to behave as a single source. The small peaks do not reflect intrinsic properties of the lattice, but are due to statistical sampling; they disappear (and reappear at other amplitudes) when the random number generator is started with a different seed value.

Effect of a visibility function on Ca^{2+} spark amplitude histograms

When the observation function is Gaussian, the Ca^{2+} spark amplitude pdf f_a, given by Eq. 30, is the sum of shifted functions of the form $(a - B)^{-1}$. The summation of the shifted functions yields a monotonically decaying function regardless of the source strength distribution f_α. We could see this monotonic behavior of f_a because we used in most of our simulations (not the ones where we detected Ca^{2+} sparks with the Ca^{2+} spark detection program) a "perfect"

detector, that is, one that detects all Ca^{2+} sparks having amplitude ≥ 1.05 while ignoring all others. This perfect detector corresponds to an infinitely steep visibility function $\psi(a)$ obtained by letting $n \rightarrow \infty$ in Eq. 31.

By setting n to finite values we obtain nonmonotonic Ca^{2+} spark amplitude distributions that look similar to those distributions obtained from actual confocal microscope measurements (see Song et al., 1997 for an exception). The observed Ca^{2+} spark amplitude pdf f_a^{obs} equals $f_a^{obs}(a) = f_a(a)\psi(a)$. Fig. 11 *A* illustrates how a nonmonotonic f_a^{obs} can arise. $f_a(a)$ (*green curve*) decreases monotonically and $\psi(a)$ (*red curve*) increases monotonically. The product f_a^{obs} (*black curve*) is nonmonotonic and is Gaussian-like. All curves are normalized so that their maximum values equal 1. To generate f_a we assumed that f_α was Gaussian with a mean of 0.5 pA and standard deviation of 0.1 pA; ψ was generated using $n = 6$ and $K_m = 1.4$. Panel *B* shows the Ca^{2+} spark amplitude histogram obtained by incorporating a visibility function in our Ca^{2+} spark generation simulations.

The Gaussian fit to the Ca^{2+} spark amplitude histogram is drawn in panel *B* (*red curve*). Note, however, that the proper "basis functions" for fitting to the amplitude histogram are hyperbolas of the form $(a - B)^{-1}$, not Gaussians.

Corresponding results derived by assuming that f_α was the sum of two Gaussians with means of 0.5 and 1 pA and standard deviation of 0.1 are shown in Fig. 11, *C* and *D*. The inflection in the f_a^{obs} curve near 1.8 occurs because sources having values ~0.5 pA no longer contribute to the population of large amplitude Ca^{2+} sparks. Fig. 11 *D* shows the Ca^{2+} spark amplitude histogram obtained by simulation using the same ψ as before. The histogram was fit to the sum of two Gaussians (*red* and *green curves*).

Effect of an asymmetric PSF on the Ca^{2+} spark amplitude distribution

Up to now we have used a symmetric PSF because it greatly simplified the analysis. To test whether violating this assumption would significantly alter our conclusions we made linescan images of identically generated Ca^{2+} sparks with a confocal microscope with asymmetric PSF. The lateral $FWHM_{x,y}$ was set to 0.2 μm and the axial $FWHM_z$ equaled 0.6 μm. The Ca^{2+} sparks were identified with the Ca^{2+} spark detection program. The amplitude histogram is shown in Fig. 12 *A*. The plot of $1/f_a^{est}$ falls on a line indicating that the amplitude histogram behaves as $(a - B)^{-1}$ just as in the cases where the PSF were symmetric. This result suggests that the conclusions drawn from assuming a symmetric PSF will not change qualitatively when the PSF is asymmetric.

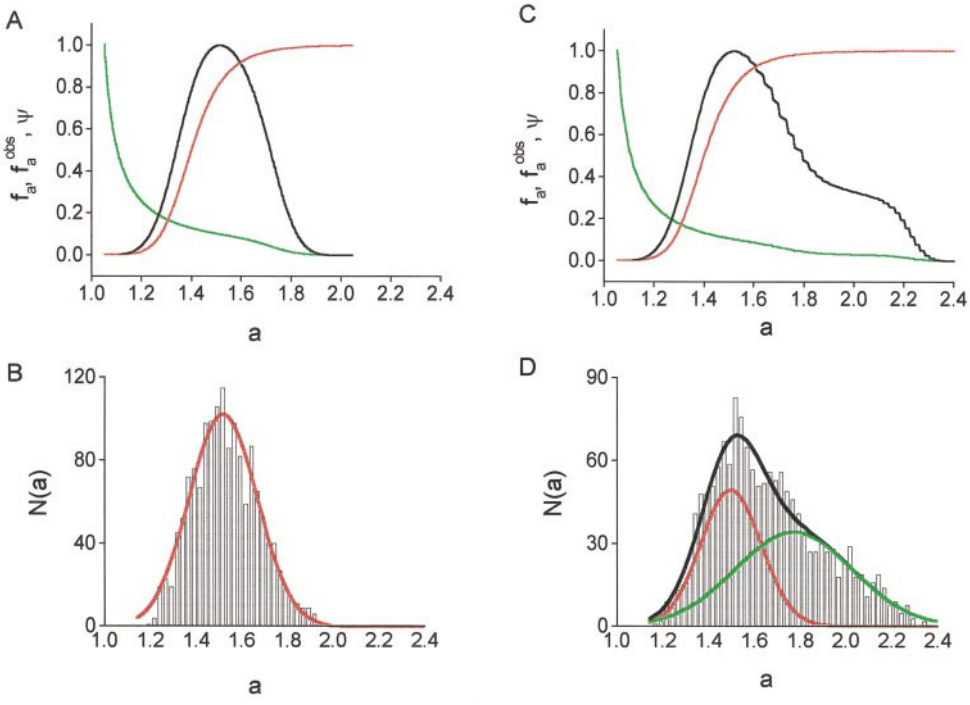

FIGURE 11 Sigmoidal visibility function transforms monotonic f_a to a Gaussian-like distribution. For (*A*) and (*B*), f_α is Gaussian with a mean of 0.5 pA and standard deviation of 0.1 pA. The observed Ca^{2+} spark amplitude distribution f_a^{obs} (*black curve*) is obtained by multiplying the theoretical f_a curve (*green curve*) by the sigmoidal visibility function (*red curve*). (*B*) Ca^{2+} spark amplitude distribution from simulations using parameters in (*A*); the red curve is a Gaussian fit to the distribution. For (*C*) and (*D*), f_α is the sum of two Gaussians with means of 0.5 and 1 pA and standard deviation of 0.1 pA for both. Curves in (*C*) have the same meaning as in (*A*). The inflection point at $a \approx 2$ in the f_a^{obs} curve arises because sources from the 0.5 pA population cannot generate Ca^{2+} sparks of amplitude >~2. The "steps" in the f_a^{obs} curve illustrate the effect of summing shifted hyperbolas; they disappear with a finer discretization of $f_\alpha(\alpha)$. (*D*) Ca^{2+} spark amplitude histogram from simulations and its fit to a sum of two Gaussians.

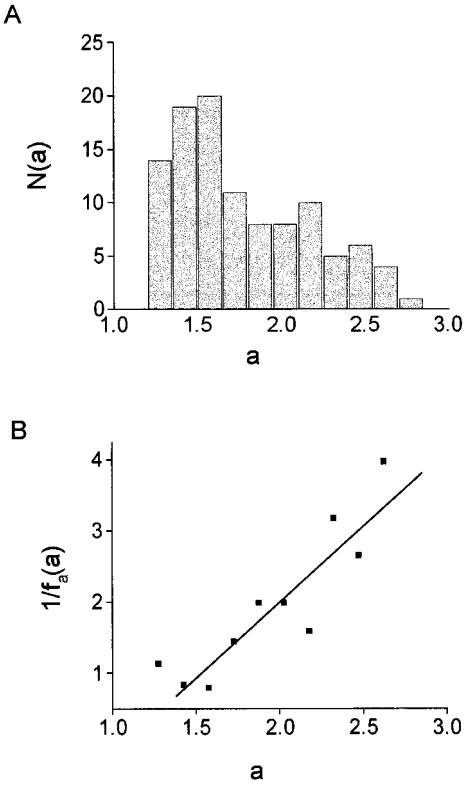

FIGURE 12 Effect of an asymmetric PSF on the Ca^{2+} spark amplitude distribution. (*A*) Ca^{2+} spark amplitude histogram obtained with $f_\alpha = \delta(\alpha - 1\ \text{pA})$ and with the axial FWHM set to 0.6 μm and the lateral $\text{FWHM}_{x,y}$ set to 0.2 μm. (*B*) Plot of $1/f_a^{est}$ is linear, indicating that the conclusions derived using a symmetric PSF are not changed qualitatively when an asymmetric PSF is used.

Effect of dye saturation on the Ca^{2+} spark amplitude distribution

When the source strength is so great that the dye becomes saturated in a broad region about the source origin, then the observation function will not be Gaussian (Eq. 20). We studied the effects that dye saturation has on the Ca^{2+} spark amplitude distribution by generating spherically symmetric sparks with a spatial profile given by

$$(G_m + G_i)(r) = \begin{cases} G_o + G_1, & 0 < r < r_o \\ G_o + G_1 \exp[-(r - r_o)^2/\sigma_r^2], & r > r_o. \end{cases} \quad (34)$$

For $0 < r < r_o = 0.5$ μm, the dye is saturated and beyond this region the Ca^{2+}-bound dye distribution decays in a Gaussian manner with space constant $\sigma_r = 0.5$ μm. The amplitude histogram (Fig. 13) no longer declines monotonically as in the previous histograms for the following reason. In the previous cases the low probability of large amplitude Ca^{2+} sparks stemmed from the need of the confocal linescan to be close to the origin. But when the dye is saturated, Ca^{2+} sparks of maximum amplitude will be detected not only when the confocal linescan is at the origin, but also when it is anywhere between 0 and r_o. Accordingly, there is a large probability of detecting large amplitude Ca^{2+} sparks.

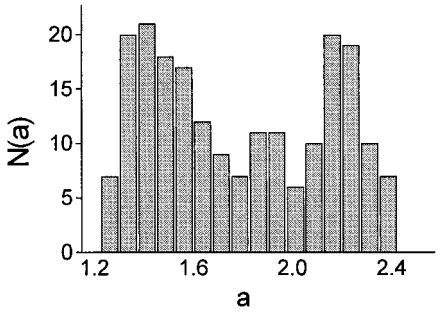

FIGURE 13 Effect of dye saturation on the Ca^{2+} spark amplitude distribution. Ca^{2+} sparks were generated with dye saturated from the center out to 0.5 μm. The spark detection program identified the Ca^{2+} sparks in the linescan images. Note that unlike previous amplitude histograms, this is nonmonotonic.

DISCUSSION

A shortcoming of using confocal microscopy to study Ca^{2+} sparks is the uncertainty of the position of the linescan relative to the origin of the Ca^{2+} spark. As Pratusevich and Balke (1996) first pointed out, the result of random placement of the linescan relative to the Ca^{2+} release site produces a broad distribution of Ca^{2+} spark amplitudes even if all the Ca^{2+} sparks were generated identically. We extended their work by addressing the important question of what would the Ca^{2+} spark amplitude distribution be if the Ca^{2+} sparks were not identically generated. The question can be posed in another way: how can we distinguish between a Ca^{2+} spark that is bright because the linescan was close to a site that released a small amount of Ca^{2+} from one that is bright, despite the linescan being far from the release site because of the large amount of Ca^{2+} released? To answer this question we addressed the following problem: given the Ca^{2+} spark amplitude distribution, what can we infer about the underlying distribution of source strengths that generate the Ca^{2+} sparks?

The main result of this paper is establishing the relationship between the source strength probability density function (pdf), f_α, and the Ca^{2+} spark amplitude pdf, f_a. The fundamental relationship between these pdf's is given by the integral equation in Eq. 19. In the specific case that $f_\alpha(\alpha)$ is a Dirac delta-function and the viewing function $g(\alpha, r)$ is Gaussian, the integral equation reduces to Eq. 26. This important equation shows that when all Ca^{2+} sparks are generated identically the measured amplitude distribution is a hyperbolic function of the form $(a - B)^{-1}$. The Ca^{2+} spark amplitude histograms in Figs. 5 *A* and 8 *C* follow this hyperbolic distribution as confirmed by the corresponding linear $1/f_a^{est}$ distribution in Figs. 5 *C* and 8 *D*. Equation 30 gives the Ca^{2+} spark amplitude pdf for arbitrary source amplitude distributions. It is seen that f_a is composed of a sum of hyperbolic functions when the viewing function is Gaussian, so f_a is monotonically declining *regardless of the source amplitude distribution*.

The monotonically declining distribution is similar to the amplitude histograms obtained by Pratusevich and Balke

(1996, Fig. 6), but stands in sharp contrast to the Ca^{2+} spark amplitude distributions from actual experiments that are often fit to a Gaussian or sums of Gaussians (Shirokova and Ríos, 1997; Xiao et al., 1997; Wier et al., 1997; Tsugorka et al., 1995). How do we reconcile these two distinct classes of Ca^{2+} spark amplitude distributions? One possibility is that the Gaussian-like distribution arises from a bias against selecting low amplitude Ca^{2+} sparks. In the theoretical development and in most of our simulations (Figs. 5 *A*, 7 *A*, 8, and 9) we have assumed that all Ca^{2+} sparks above some minimum amplitude are detected with perfect reliability. In practice this perfect reliability is unlikely to be achieved by humans or even by automatic Ca^{2+} spark detectors, as seen in Fig. 5, *A* and *B*. In Fig. 5 *B* there are more Ca^{2+} sparks in the second nonempty bin than in the first, indicating a greater probability of detecting the larger amplitude Ca^{2+} sparks. By assuming a sigmoidal visibility function (Pratusevich and Balke, 1996), which gives the statistical reliability of detecting a Ca^{2+} spark of a given amplitude, we obtained a Gaussian-like Ca^{2+} spark amplitude distribution even when the actual Ca^{2+} spark amplitude distribution declines monotonically, as shown in Fig. 11, *A* and *B*.

Support for this explanation comes from Song et al. (1997) who identified Ca^{2+} sparks from rat ventricular cells using a computer algorithm instead of by eye. They measured the visibility function of their detection algorithm, then used the visibility function to correct for undetected small amplitude Ca^{2+} sparks. By making this correction, Song et al. obtained a Ca^{2+} spark amplitude distribution that declined virtually monotonically, as predicted from our analysis.

Apart from selection bias, we identified two other ways that a nonmonotonic Ca^{2+} spark amplitude distribution can arise by violating some of the assumptions underlying the derivation of Eq. 30. One assumption was that the observation function is a strictly monotonic function of r. This assumption is violated when the source strength is large enough that the Ca^{2+} spark generated has a broad region of saturation. In this case the Ca^{2+} spark amplitude distribution can be nonmonotonic, as shown in Fig. 13.

Although it would be tempting to interpret Fig. 13 as indicative of two populations of Ca^{2+} sparks, our previous results on multiple spark populations cautions against such an interpretation. It is not always easy to know when the dye is saturated. Even if there is a broad region of dye saturation, a Ca^{2+} spark spatial profile may still appear Gaussian if the linescan was sufficiently far from the source. Only the spatial profiles of the brightest sparks might show the "flat top" signature of saturation.

There is another way of getting a Gaussian or any Ca^{2+} spark amplitude distribution even with a perfect detector, but it requires an unlikely assumption. In calculating $f_a(a)$ using Eq. 26 or Eq. 30, R was set to a distance at which the Ca^{2+} spark amplitude will be close to the threshold for detection (typically 1.05). If R is set to a much smaller value, such as might occur *if fluo-3 were physically prevented from diffusing beyond a certain point*, then f_a takes on the appearance of the source amplitude distribution f_α. To see this, consider an extreme example. Suppose that the t-tubule–SR junction acted as a giant sink for fluo-3, resulting in zero fluorescence except at these junctions. Then any recorded Ca^{2+} spark necessarily comes from a position $r \approx 0$ and the Ca^{2+} spark amplitude will be $\approx a_{max}(\alpha)$. Thus the Ca^{2+} spark amplitude distribution will simply mirror the distribution of α.

We now point out what will *not* produce, in general, a nonmonotonic Ca^{2+} spark amplitude distribution. One assumption we made is that the Ca^{2+} release site could be anywhere with respect to the linescan with equal probability. Under this assumption the distance pdf is $f_r(r) = 2r/R^2$. This assumption is not satisfied in actual cells since SR Ca^{2+} release sites are restricted to the t-tubule–SR junction. Pratusevich and Balke (1996) have already shown that when Ca^{2+} sparks were generated identically at sites arranged on a regular lattice and viewed from a fixed linescan position, the amplitude histogram was neither monotonically declining nor Gaussian, but showed distinct peaks. We carried out a similar calculation confirming their results (data not shown) demonstrating that when the assumption that Ca^{2+} sparks can arise anywhere relative to the linescan position is violated, the Ca^{2+} spark amplitude histogram is nonmonotonic.

However, Ca^{2+} spark amplitude histograms are not usually constructed from results from a single cell, so we simulated the experiment where there were 20 or 200 cells. For each cell the linescan position was at a fixed, but random, point in a regular square lattice of release sites. As a result of the randomization of the linescan position the Ca^{2+} spark amplitude distribution for the combined data from the 20 or 200 cells do not show distinctive peaks (Fig. 10, *A* and *D*). In fact, the distribution of distances between linescan position and release sites (Fig. 10, *C* and *F*) falls precisely on the line $f_r(r) = 2r/R^2$. Thus even when the release sites are not at arbitrary distances from the linescan position, the effect of using a moderate-to-large number of cells is to make it appear that the release sites are arbitrarily and uniformly distributed about the linescan position.

As a result, when many linescan images are taken from only a few cells ($\sim$5), peaks in the amplitude histogram may appear that reflect the spatial distribution of Ca^{2+} release sites, as pointed out by Pratusevich and Balke (1996). Their cautionary note about interpreting these peaks as representing different populations should be heeded when only a small number of cells are used. However, these peaks in the histograms are expected to disappear when a moderate number of cells ($\sim$20) are used or there is variability in the arrangement of Ca^{2+} release sites, i.e., the release sites are not on a perfectly regular lattice in the y–z plane.

Interpreting the Ca^{2+} spark amplitude histogram

The Ca^{2+} spark amplitude histogram $N(a)$ contains the information needed to calculate the probability distribution of source strengths f_α. According to Eq. 30 the relationship

between $N(a)$ [or equivalently $f_a(a)$, see Eq. 28] and f_α is most clearly seen when the reciprocal of $N(a)$ is plotted against the Ca^{2+} spark amplitude a. If a plot of $1/N(a)$ yields a straight line, then it implies that the Ca^{2+} sparks come from a single population of release sites. The source strength α is calculated using the largest Ca^{2+} spark amplitude a_{max}. In practice because of the visibility function, the number of small amplitude events will be underrepresented so only values of a beyond the initial rising part of the histogram should be used.

If the source strengths are normally distributed about a single mean, as might be expected from small variations in loading (Satoh et al., 1997), for example, then $1/N(a)$ will be initially linear, then rise sharply at large amplitudes, as shown in Fig. 8 *B*. In practice, the large amount of scatter at the larger amplitudes may make it difficult to distinguish between f_α that is a Dirac delta-function from a Gaussian distribution, as seen in Fig. 8, *B* and *D*. This example illustrates a general difficulty. In many cases, the difference between various source strength populations show up near the tail of the Ca^{2+} spark amplitude distribution, where the numbers of Ca^{2+} sparks are small. Accordingly, the scatter in the $1/N(a)$ plot is great for large amplitudes. This points to the need to record large numbers of Ca^{2+} sparks to carry out the analysis shown in this paper.

We used our model results to interpret a Ca^{2+} spark amplitude distribution from an actual experiment of Song et al. (1997), Fig. 9 *C*. We used their data because 1) they had a fairly large number of Ca^{2+} sparks in their sample ($N_{total} = 751$); 2) the Ca^{2+} sparks were identified not by eye, but by using a computer algorithm, which reduced selection bias; and 3) they compensated for their system's detection efficiency (equivalent to our visibility function), thereby approximating a perfect detector. Thus, their experiment approximates our simulations. The good fit to the data suggests that the Ca^{2+} sparks were generated by SR Ca^{2+} release channels carrying 1.4 pA and having exponentially distributed open times with a mean of 6 ms. We believe that this is the first instance of a theory-based interpretation of a Ca^{2+} spark amplitude histogram.

Detecting multiple Ca^{2+} spark populations

Multiple populations of Ca^{2+} sparks have been reported to arise from multiple conductance states of the Ca^{2+} release channel (Xiao et al., 1997), by triggering of neighboring release sites (Klein et al., 1996), or differences in SR load (Satoh et al., 1997; Györke et al., 1997). Our results suggest a method for distinguishing these multiple populations. Fig. 7, *A* and *B* show the Ca^{2+} spark amplitude histograms derived from Ca^{2+} sparks generated by sources carrying two different currents. There is nothing striking in the histograms suggesting that the Ca^{2+} sparks arose from two populations. The drop in the number of Ca^{2+} sparks at $a \approx 2.2$ is real, but can be easily overlooked as simply statistical fluctuations. Alternatively, a plot of $1/f_a(a)$ clearly reveals two population of Ca^{2+} sparks evidenced by the discontinuity at $a \approx 2.2$.

Note that the plot of $1/f_a(a)$ "automatically" distinguishes between intrinsically small Ca^{2+} sparks and those that have small amplitudes simply because they arose far from the linescan. The two source amplitudes α_1 and α_2 that generated these two Ca^{2+} spark populations are calculated from the Ca^{2+} spark amplitude at the discontinuity $a_{max}(\alpha_1)$ and the largest observed amplitude $a_{max}(\alpha_2)$. These values do not correspond to the peaks of the Gaussian curves that can be fit to the Ca^{2+} spark amplitude distributions; using the amplitudes at the peaks will underestimate the source strength values. Moreover, multiple Gaussian fits to the Ca^{2+} spark amplitude histograms can be misleading. Fig. 11 *D* shows a Ca^{2+} spark amplitude histogram fit to two Gaussians. This figure suggests that population of Ca^{2+} sparks generated by the larger amplitude sources (*green curve*) makes a relatively small contribution to the small amplitude Ca^{2+} sparks. In fact, the opposite is true. For any given Ca^{2+} spark amplitude, Ca^{2+} sparks generated by sources of greater strength can be detected by more distant linescans, so are expected to be more numerous than Ca^{2+} sparks generated by sources of lower strength.

Limitations

Limitations of our work come from simplifying assumptions made in 1) modeling the Ca^{2+} spark generation and 2) establishing the relationship between the Ca^{2+} spark amplitude and source strength distributions. The important assumption made in 2) is that the confocal microscope's PSF is spherically symmetric. This simplifying assumption is both the strength and weakness of our analysis. By virtue of its simplicity, the essential principles that underlie the relationship between the Ca^{2+} spark amplitude histogram and the source strength distribution could be laid bare. This relationship could be found analytically (Eq. 30), thus allowing us to exactly calculate the effects that different source strength distributions have on the Ca^{2+} spark amplitude histogram. Without the simplifying assumption of spherical symmetry we would have needed to resort to a numerical solution of an integral equation that was more complicated than Eq. 19. The results might be more accurate but less insightful. The weakness of this assumption is, of course, that no confocal microscope has a spherically symmetric PSF. Fig. 12 shows that when an asymmetric PSF is used, a plot of $1/f_a$ still yields a straight line when f_α is a Dirac delta-function. Thus we do not think that the results of our analysis would change qualitatively by dropping the spherically symmetric assumption.

A number of simplifications were made in modeling the reaction and diffusion of Ca^{2+}. We did not include Ca^{2+} pumps because the results of Gómez et al. (1996) show that most of the decline in the dye fluorescence is attributable to diffusion and buffering. We have also lumped the different endogenous buffers into a single composite buffer. These

simplifications need to be relaxed to gain a more thorough understanding of Ca^{2+} dynamics and Ca^{2+} spark properties. [These simplifications are not made in the paper by Smith et al. (1998).] Given that the viewing function could be fit to a Gaussian (Eq. 20) whether β was 2 or 5 or whether α was the channel current or the channel open time, suggests that the form of the observation function is robust and unlikely to change qualitatively as the models for Ca^{2+} spark generation change. Thus, as better models of Ca^{2+} spark generation are developed the viewing function $g(\alpha, r)$ can be refined and more accurate relationships between the Ca^{2+} spark amplitude and source strength distributions will evolve using the framework developed here.

The authors thank Dr. Ye Chen (National Institutes on Aging, NIH) and Dr. Robert Spangler (SUNY at Buffalo) for insightful discussions; Dr. Heping Cheng (National Institutes on Aging, NIH) and colleagues for a preprint of their spark modeling paper; and Dr. Cheng for access to the code for his automatic spark detector.

REFERENCES

Balke, C. W., T. M. Egan, and W. G. Wier. 1994. Processes that remove calcium from the cytoplasm during excitation-contraction coupling in intact rat heart cells. *J. Physiol.* 474:447–462.

Berlin, J. R., J. W. M. Bassani, and D. M. Bers. 1994. Intrinsic cytosolic calcium buffering properties of single rat cardiac myocytes. *Biophys. J.* 67:1775–1787.

Blatter, L. A., J. Hüser, and E. Rios. 1997. Sarcoplasmic reticulum Ca^{2+} release flux underlying Ca^{2+} sparks in cardiac muscle. *Proc. Natl. Acad. Sci. USA.* 94:4176–4181.

Blatter, L. A., and W. G. Wier. 1990. Intracellular diffusion, binding, and compartmentalization of the fluorescent calcium indicators indo-1 and fura-2. *Biophys. J.* 58:1491–1499.

Cannell, M. B., H. Cheng, and W. J. Lederer. 1995. The control of calcium release in heart muscle. *Science.* 268:1045–1049.

Cheng, H., W. J. Lederer, and M. B. Cannell. 1993. Calcium sparks: elementary events underlying excitation-contraction coupling in heart muscle. *Science.* 262:740–744.

Gómez, A. M., H. Cheng, W. J. Lederer, and D. M. Bers. 1996. Ca^{2+} diffusion and sarcoplasmic reticulum transport both contribute to $[Ca^{2+}]_i$ decline during Ca^{2+} sparks in rat ventricular myocytes. *J. Physiol.* 496:575–581.

Györke, S., V. Lukyanenko, and I. Györke. 1997. Dual effects of tetracaine on spontaneous calcium release in rat ventricular myocytes. *J. Physiol.* 500:297–309.

Hague, D. N. 1977. Dynamics of substitution at metal ions. *In* Chemical Relaxation in Molecular Biology. I. Pecht and R. Rigler, editors. Springer-Verlag, Berlin. 84–106.

Harkins, A. B., N. Kurebayashi, and S. M. Baylor. 1993. Resting myoplasmic free calcium in frog skeletal muscle fibers estimated with fluo-3. *Biophys. J.* 65:865–881.

Klein, M. G., H. Cheng, L. F. Santana, Y.-H. Jiang, W. J. Lederer, and M. F. Schneider. 1996. Two mechanisms of quantized calcium release in skeletal muscle. *Nature.* 379:455–458.

Lipp, P., and E. Niggli. 1996. Submicroscopic calcium signals as fundamental events of excitation-contraction coupling in guinea-pig cardiac myocytes. *J. Physiol.* 492:31–38.

López-López, J. R., P. S. Shacklock, C. W. Balke, and W. G. Wier. 1994. Local, stochastic release of Ca^{2+} in voltage-clamped rat heart cells: visualization with confocal microscopy. *J. Physiol.* 480:21–29.

López-López, J. R., P. S. Shacklock, C. W. Balke, and W. G. Wier. 1995. Local calcium transients triggered by single L-type calcium channel currents in cardiac cells. *Science.* 268:1042–1045.

Lukyanenko, V., I. Györke, and S. Györke. 1996. Regulation of calcium release by calcium inside the sarcoplasmic reticulum in ventricular myocytes. *Pflügers Arch.–Eur. J. Physiol.* 432:1047–1054.

Nelson, M. T., H. Cheng, M. Rubart, L. F. Santana, A. D. Bonev, H. J. Knot, and W. J. Lederer. 1995. Relaxation of arterial smooth muscle by calcium sparks. *Science.* 270:633–637.

Parker, I., N. Callamaras, and W. G. Wier. 1997. A high-resolution, confocal laser-scanning microscope and flash photolysis system for physiological studies. *Cell Calcium.* 21:441–452.

Parker, I., and W. G. Wier. 1996. Ca^{2+} sparks studied by stationary point confocal femtofluorimetry. *J. Mol. Cell. Cardiol.* 28:A132.

Parker, I., W.-J. Zang, and W. G. Wier. 1996. Ca^{2+} sparks involving multiple Ca^{2+} release sites along Z-lines in rat heart cells. *J. Physiol.* 497:31–38.

Pawley, J. 1995. Fundamental limits in confocal microscopy. *In* Handbook of Biological Confocal Microscopy. J. B. Pawley, editor. Plenum Press, New York. 19–37.

Pratusevich, V. R., and C. W. Balke. 1996. Factors shaping the confocal image of the calcium spark in cardiac muscle cells. *Biophys. J.* 71: 2942–2957.

Rousseau, E., and G. Meissner. 1989. Single cardiac sarcoplasmic reticulum Ca^{2+} release channel: activation by caffeine. *Am. J. Physiol.* 256: H328–H333.

Santana, L. F., H. Cheng, A. M. Gómez, M. B. Cannell, and W. J. Lederer. 1996. Relation between the sarcolemmal Ca^{2+} current and Ca^{2+} sparks and local control theories for cardiac excitation-contraction coupling. *Circ. Res.* 78:166–171.

Satoh, H., L. A. Blatter, and D. M. Bers. 1997. Effects of $[Ca^{2+}]$, SR Ca^{2+} load, and rest on Ca^{2+} spark frequency in ventricular myocytes. *Am. J. Physiol.* 242:H657–H668.

Shacklock, P. S., W. G. Wier, and C. W. Balke. 1995. Local Ca^{2+} transients (Ca^{2+} sparks) originate at transverse tubules in rat heart cells. *J. Physiol.* 487:601–608.

Shirokova, N., and E. Ríos. 1997. Small event Ca^{2+} release: a probable precursor of Ca^{2+} sparks in frog skeletal muscle. *J. Physiol.* 502:3–11.

Shorofsky, S. R., L. Izu, W. G. Wier, and C. W. Balke. 1998. Ca^{2+} sparks triggered by patch depolarization in rat heart cells. *Circ. Res.* 82: 424–429.

Shorofsky, S. R., P. S. Shacklock, W. G. Wier, and C. W. Balke. 1996. Multiple populations of calcium sparks in rat ventricular cells. *Circulation.* 94:A0917.

Shorofsky, S. R., W. G. Wier, and C. W. Balke. 1997. Calcium sparks in spontaneously hypertensive rats with cardiac hypertrophy. *Biophys. J.* 72:A343.

Smith, G. D., J. E. Keizer, M. D. Stern, W. J. Lederer, and H. Cheng. 1998. A simple numerical model of calcium spark formation and detection in cardiac myocytes. *Biophys. J.*, in press.

Smith, G. D., J. Wagner, and J. Keizer. 1996. Validity of the rapid buffering approximation near a point source of calcium ions. *Biophys. J.* 70:2527–2539.

Song, L.-S., M. D. Stern, E. G. Lakatta, and H. Cheng. 1997. Partial depletion of sarcoplasmic reticulum calcium does not prevent calcium sparks in rat ventricular myocytes. *J. Physiol.* 505:665–675.

Stern, M. D. 1992. Theory of excitation-contraction coupling in cardiac muscle. *Biophys. J.* 63:497–517.

Tsugorka, A., E. Ríos, and L. A. Blatter. 1995. Imaging elementary events of calcium release in skeletal muscle cells. *Science.* 269:1723–1726.

Wagner, J., and J. Keizer. 1994. Effects of rapid buffers on Ca^{2+} diffusion and Ca^{2+} oscillations. *Biophys. J.* 67:447–456.

Wier, W. G., H. E. D. J. ter Keurs, E. Marban, W. D. Gao, and C. W. Balke. 1997. Ca^{2+} "sparks" and waves in intact ventricular muscle resolved by confocal imaging. *Circ. Res.* 81:462–469.

Xiao, R.-P., H. H. Valdivia, K. Bogdanov, C. Valdivia, E. G. Lakatta, and H. Cheng. 1997. The immunophilin FK506-binding protein modulates Ca^{2+} release channel closure in rat heart. *J. Physiol.* 500:343–354.